

## Crystal Systems and Lattice Parameters of $\text{CH}_3\text{NH}_3\text{Pb}(\text{I}_{1-x}\text{Br}_x)_3$ Determined Using Single Crystals: Validity of Vegard's Law

Yuiga Nakamura, Naoyuki Shibayama,\* Akiko Hori, Tomonori Matsushita, Hiroshi Segawa,\* and Takashi Kondo\*



Cite This: *Inorg. Chem.* 2020, 59, 6709–6716



Read Online

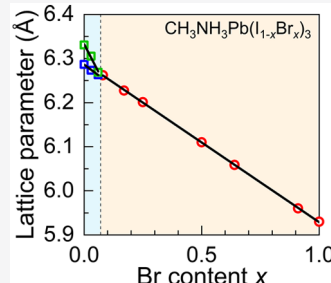
ACCESS |

Metrics & More

Article Recommendations

Supporting Information

**ABSTRACT:** Metal halide perovskites are promising materials for light absorbers in solar cell applications. Use of the Br/I system enables us to control band gap energy and improves the efficiency of solar cells. Precise knowledge of lattice parameters and band gap energies as functions of compositions are crucially important for developing the devices using those materials. In this study, we have determined lattice parameters and band gap energies of  $\text{CH}_3\text{NH}_3\text{Pb}(\text{I}_{1-x}\text{Br}_x)_3$ , one of the most intensively studied mix-halide perovskites, as functions of Br content  $x$ . We measured accurate Br contents and lattice parameters of  $\text{CH}_3\text{NH}_3\text{Pb}(\text{I}_{1-x}\text{Br}_x)_3$  ( $0 \leq x \leq 1$ ) using single-crystalline samples by X-ray photoelectron spectroscopy (XPS) and X-ray diffraction (XRD) measurements, respectively. The  $\text{CH}_3\text{NH}_3\text{Pb}(\text{I}_{1-x}\text{Br}_x)_3$  crystal system is tetragonal for  $x \leq 0.06$  and cubic for  $x \geq 0.08$  at 300 K. Lattice parameters of  $\text{CH}_3\text{NH}_3\text{Pb}(\text{I}_{1-x}\text{Br}_x)_3$  strictly follow Vegard's law; i.e., they are linearly dependent on  $x$ . We give linear expressions of  $x$  of lattice parameters for the tetragonal and cubic phases of  $\text{CH}_3\text{NH}_3\text{Pb}(\text{I}_{1-x}\text{Br}_x)_3$  at 300 K. We have shown that these expressions can be used for determining the Br contents of  $\text{CH}_3\text{NH}_3\text{Pb}(\text{I}_{1-x}\text{Br}_x)_3$  polycrystalline thin-film samples based on XRD measurements and, in addition, demonstrated that XPS measurements on polycrystalline samples may be erroneous because of impure ingredients in the samples. Furthermore, we determined band gap energies of  $\text{CH}_3\text{NH}_3\text{Pb}(\text{I}_{1-x}\text{Br}_x)_3$  ( $0 \leq x \leq 1$ ) at room temperature using absorption spectra of polycrystalline thin films taking account of excitonic effects.



### INTRODUCTION

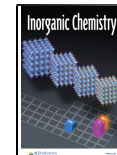
Metal halide perovskites have attracted considerable attention since the rediscovery as materials for solar cells in 2009.<sup>1</sup> The highest power conversion efficiency of the perovskite solar cells has already exceeded 25% which is higher than those of practical thin-film solar cells such as Si, CdTe, and CIGS.<sup>2</sup> This tremendous success is owed to the outstanding properties of lead halide perovskites including strong light absorption and long lifetimes of charge carriers exhibiting recombination rates as low as those of high-quality inorganic semiconductors.<sup>3</sup> Because of these fascinating features, lead halide perovskites have been investigated also for applications to electro-optic devices, such as photodetectors,<sup>4–6</sup> light-emitting diodes,<sup>7</sup> and lasers.<sup>8</sup>

One of the perovskites most widely investigated to date is  $\text{CH}_3\text{NH}_3\text{PbI}_3$  (MAPbI<sub>3</sub>) which is considered as the baseline for subsequent changes.<sup>9</sup> For the applications described above, tunabilities of band gap energies are crucially important. While modifications on A-site cations (replacing methylammonium (MA) cations with formamidinium or Cs cations) lead to slight band gap energy shifts typically of the order of 0.1 eV,<sup>10–14</sup> halide anion mixings result in much larger band gap energy changes of the order of 1 eV. For example, band gap energies of MAPb(I<sub>1-x</sub>Br<sub>x</sub>)<sub>3</sub> cover a wide spectrum range; the absorption edge energy of MAPb(I<sub>1-x</sub>Br<sub>x</sub>)<sub>3</sub> changes from about 1.5 eV (that of MAPbI<sub>3</sub>) to about 2.3 eV (that of

MAPbBr<sub>3</sub>) depending on the Br/I ratio.<sup>15</sup> In addition, lattice constants of perovskite alloys are also very important because most researchers determine the alloy compositions using lattice constants measured by X-ray diffraction relying on previously reported relations between alloy compositions and lattice parameters. However, reliable composition-lattice constant relations have not been established for halide perovskites to date, unfortunately. Even for MAPb(I<sub>1-x</sub>Br<sub>x</sub>)<sub>3</sub>, one of the most thoroughly investigated mixed-halide perovskites, we have no standard values of lattice parameters as functions of the Br content  $x$ . The most important objective of our present study is to establish a precise relation between lattice parameters and Br content in MAPb(I<sub>1-x</sub>Br<sub>x</sub>)<sub>3</sub>. Lattice parameters of MAPb(I<sub>1-x</sub>Br<sub>x</sub>)<sub>3</sub> have been measured by a number of researchers using polycrystalline thin-film samples<sup>16–21</sup> and powder samples obtained by grinding single crystals.<sup>22,23</sup> The main difficulty comes from inaccuracy in Br content determination. Noh et al. assumed that Br contents of MAPb(I<sub>1-x</sub>Br<sub>x</sub>)<sub>3</sub> polycrystalline films were the same as those of precursor

Received: November 22, 2019

Published: March 18, 2020



solutions in determining  $x$ -dependent lattice parameters.<sup>16</sup> However, this composition determination is highly risky; polycrystalline film compositions are reported to depend on the preparation methods probably due to existence of impurities or material loss during the preparation process.<sup>17</sup> Direct composition analyses can also be erroneous for polycrystalline and powder samples because the existence of impurities such as  $\text{PbI}_2$  leads to significant errors. It should be noted that unusual nonstoichiometry in  $\text{MAPb}(\text{I}_{1-x}\text{Br}_x)_3$  polycrystalline samples (presumably an apparent deviation from the stoichiometry due to impurities) are reported.<sup>24</sup> Actually, previously reported data of  $x$ -dependent lattice parameters significantly differ from one another as shown in Figure S1. Moreover, considerable scattering of data can be seen even for each data set which makes it difficult to discuss on the validity of Vegard's law (linear dependence of the lattice parameters on  $x$ ). Although the validity of Vegard's law<sup>17</sup> and negative deviation from Vegard's law<sup>18</sup> have been reported, their conclusions cannot be justified due to limited accuracies in their experimental data. The validity of Vegard's law, in fact, is very important for understanding interatomic interactions between halide anions, because negative/positive deviation from the linear  $x$ -dependence of the lattice parameters indicates attractive/repulsive interaction between neighboring I and Br anions<sup>25</sup> which, in turn, affects the mechanical properties and thermodynamic stabilities of this material. In addition, precise knowledge of the crystal system as a function of the Br content  $x$  is also important, because there has been no consensus on the boundary between I-rich tetragonal and Br-rich cubic phases as is readily seen in Figure S1.

In this study, we measured Br contents  $x$ , crystal systems, and lattice parameters of  $\text{MAPb}(\text{I}_{1-x}\text{Br}_x)_3$  by using mixed-halide single crystalline samples which enabled us to determine the  $x$ -dependent crystal system and lattice parameters with satisfactory accuracies and to discuss the validity of Vegard's law in this material system. In addition, we investigated  $\text{MAPb}(\text{I}_{1-x}\text{Br}_x)_3$  polycrystalline thin films and compared Br contents determined by lattice constant measurements and direct composition analyses. Based on spectroscopic measurement on polycrystalline thin films, we determined  $x$ -dependent band gap energies of  $\text{MAPb}(\text{I}_{1-x}\text{Br}_x)_3$  taking account of excitonic effects.

## EXPERIMENTAL SECTION

**Material.** All solvents and chemicals were purchased and used as obtained.  $\gamma$ -Butyrolactone (GBL), *N,N*-dimethylformamide (DMF), and dimethyl sulfoxide (DMSO) were purchased from Kanto Chemical Co., Inc. MAI, MABr, and  $\text{PbBr}_2$  were purchased from TCI Co., Ltd.  $\text{PbI}_2$  (99.99%) was obtained from Kojundo Chemical Laboratory Co., Ltd. All solvents and reagents were of the highest quality available and were used as received.

**Growth of  $\text{MAPb}(\text{I}_{1-x}\text{Br}_x)_3$  Single Crystals.** The solvent evaporation method was employed in a class 10,000 cleanroom with a 22 °C–40 RH% to grow dual-halide  $\text{MAPb}(\text{I}_{1-x}\text{Br}_x)_3$  single crystals. A GBL solution (1.3 M) of  $\text{MAPbI}_3$  was prepared by dissolving  $\text{PbI}_2$  and MAI with a molar ratio of 1:1 into GBL. A DMF solution (0.7 M) of  $\text{MAPbBr}_3$  was prepared by dissolving  $\text{PbBr}_2$  and MABr with a molar ratio of 1:1 into DMF. All solutions were filtered using a hydrophilic polytetrafluoroethylene (PTFE) membrane filter (28HP04SAN, Advantec Toyo Kaisha, Ltd.). For growing  $\text{MAPb}(\text{I}_{1-x}\text{Br}_x)_3$  single crystals, measured volumes of  $\text{MAPbI}_3$  and  $\text{MAPbBr}_3$  solution were mixed to form the precursor solution with the desired Br:I ratio (Table S1). The  $\text{MAPb}(\text{I}_{1-x}\text{Br}_x)_3$  solutions were heated and kept at 100 °C, and left for 2 days until  $\text{MAPb}(\text{I}_{1-x}\text{Br}_x)_3$  single crystals with typical dimensions of about 2 mm were formed. Finally, we

selected the highest quality single crystal from each solution, and washed the selected single crystals using  $\text{CH}_2\text{Cl}_2$ .

### Preparation of $\text{MAPb}(\text{I}_{1-x}\text{Br}_x)_3$ Polycrystalline Thin Films.

DMF/DMSO solutions of  $\text{MAPbI}_3$  and  $\text{MAPbBr}_3$  (1.3 M) were prepared by dissolving  $\text{PbI}_2 + \text{MAI}$  and  $\text{PbBr}_2 + \text{MABr}$  with a molar ratio of 1:1 into the DMF/DMSO (4:1 in volume) solvent, respectively. The prepared solutions of  $\text{MAPbI}_3$  and  $\text{MAPbBr}_3$  were mixed to obtain the  $\text{MAPb}(\text{I}_{1-x}\text{Br}_x)_3$  solution with desired Br:I ratio. The nonalkaline glass substrates were cleaned ultrasonically with detergent, distilled water, and ethanol, and treated with  $\text{O}_3$  for 15 min to eliminate organic impurities and to make the surface clean. A solution of  $\text{MAPb}(\text{I}_{1-x}\text{Br}_x)_3$  was spin-coated on the nonalkaline glass substrates at 1000 rpm for 10 s and at 4000 rpm for 30 s, subsequently, inside a drying room with a dew-point temperature of –30 °C. During the spin coating, toluene was dripped on the perovskite layer. The film was annealed at 60 °C for 10 min, and then at 100 °C for 15 min. Details of the polycrystalline film fabrication process have been described elsewhere.<sup>26,27</sup>

**Characterization of Single Crystals.** For determining Br contents, we employed X-ray photoemission spectroscopy (XPS). In all the XPS measurements, single crystals were cleaved immediately before the measurement and quickly transferred to the XPS chamber. The X-ray probe was incident on the fresh cleaved surfaces near the center of the single-crystalline sample. XPS data were acquired using a spectrophotometer (PHI 5000 VersaProbe, ULVAC, Inc.) with a monochromatic Al  $\text{K}\alpha$  X-ray source (1486.6 eV), and the energy offset was calibrated using the C 1s peak of contaminant carbon as a reference at 284.8 eV.

We determined crystal systems, lattice parameters, and crystal structures by single crystal X-ray diffraction (SC-XRD) measurements using a Bruker D8 Quest diffractometer with a Photon II using Mo $\text{K}\alpha$  radiation ( $\lambda = 0.71073 \text{ \AA}$ ) generated at 50 kV and 1 mA. The single-crystalline samples with typical dimensions of  $0.1 \times 0.1 \times 0.1 \text{ mm}^3$  were prepared from the center of the single crystals used for the XPS measurements and were mounted on glass fibers. All the SC-XRD measurements were performed at 300 K using a temperature-controlled dry nitrogen gas flow. After determining the crystal systems considering the extinction rule, we refined the lattice parameters. The SHELXT program was used for solving the structures.<sup>28</sup> Refinement and further calculations were carried out using SHELXL.<sup>29</sup> The detailed treatment of disorder atoms in SC-XRD analysis is described in the Supporting Information.

**Characterization of Polycrystalline Thin Films.** For measuring lattice parameters, we used two-dimensional wide-angle X-ray scattering (2D-WAXS) analysis<sup>30</sup> in order to exclude orientation effects. 2D-WAXS measurement was conducted at an X-ray incident angle of 5° and photon energy of 12.39 keV (1.0  $\text{\AA}$ ) by using synchrotron radiation at beamline BL19B2 of SPring-8 equipped with a PILATUS 300K, two-dimensional (2D) X-ray detector. All the measurements were performed at room temperature (296 K). The scattering patterns  $I_{2D}(q, \chi)$  measured by the 2D detector were azimuthally integrated to obtain the one-dimensional (1D) intensity profiles  $I_{1D}(q)$  as follows:

$$I_{1D}(q) = \frac{1}{2\pi} \int_0^{2\pi} I_{2D}(q, \chi) d\chi$$

where  $q$  is the magnitude of the scattering vector and  $\chi$  is the azimuthal angle.

XPS measurements on polycrystalline samples were performed as in the case for single-crystalline samples described above.

UV-vis absorption spectroscopy was performed using a Hitachi UH-4150 spectrophotometer for measuring absorption spectra of polycrystalline films. All the absorption measurements were conducted at room temperature (296 K).

## RESULTS AND DISCUSSION

**Single Crystals.** Figure 1 shows 10  $\text{MAPb}(\text{I}_{1-x}\text{Br}_x)_3$  single crystalline samples we selected for each  $x$ . The Br contents indicated in Figure 1 are values determined by XPS. Mixing

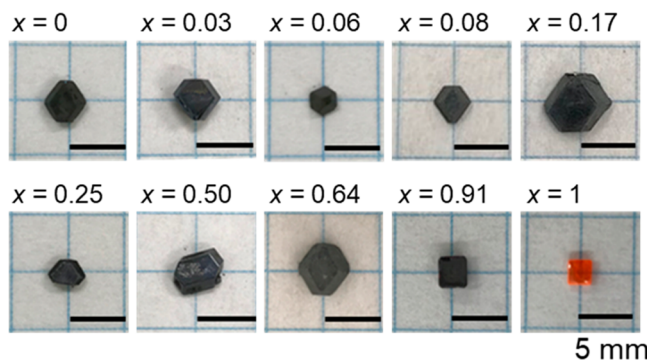


**Figure 1.** Photographs of MAPb(I<sub>1-x</sub>Br<sub>x</sub>)<sub>3</sub> single-crystalline samples ( $x = 0\text{--}1$ ).

ratios of the mother solutions used for growing these crystals are summarized in **Table S1**. As the Br content increased, the color of MAPb(I<sub>1-x</sub>Br<sub>x</sub>)<sub>3</sub> turns from black to orange, as shown in **Figure 1**. Furthermore, with increasing Br content, the crystal shape transforms from dodecahedral, typical for low- $x$  MAPb(I<sub>1-x</sub>Br<sub>x</sub>)<sub>3</sub> single crystals dominated by {110}<sub>c</sub> planes, to hexahedral, typical for high- $x$  MAPb(I<sub>1-x</sub>Br<sub>x</sub>)<sub>3</sub> single crystals dominated by {100}<sub>c</sub> planes, because of the change in surface energies.<sup>31</sup> The colors and shapes of these single-crystalline samples are consistent with those previously reported.<sup>23</sup>

We performed XPS measurements on 10 single-crystalline samples (XPS spectra are shown in **Figures 2** and **S2–S5**). All the numerical results are summarized in **Table S2**. We have confirmed that (Br + I):Pb ratios for all the sample agreed with the stoichiometric value 3:1. Observed chemical shifts were negligible for the peaks observed, suggesting that these

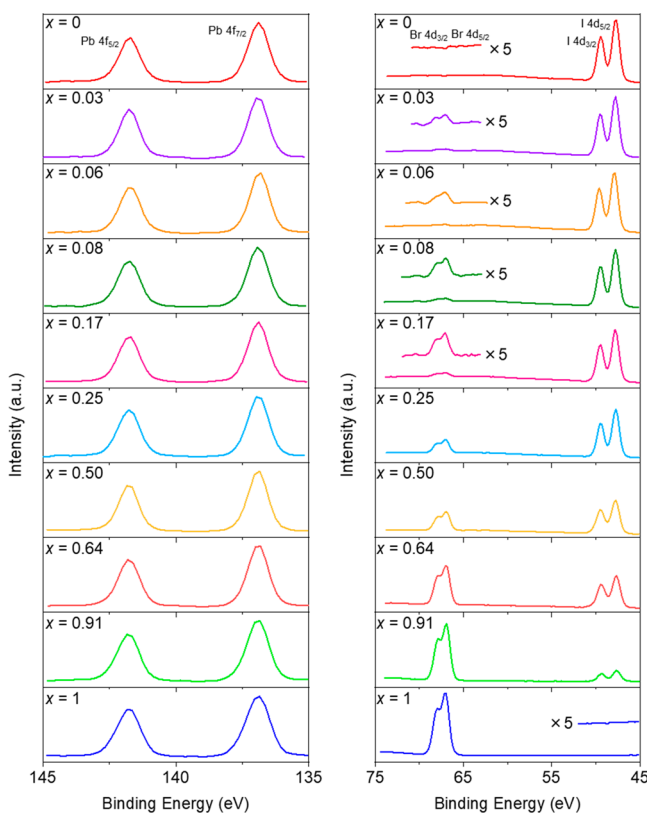


**Figure 2.** XPS spectra of MAPb(I<sub>1-x</sub>Br<sub>x</sub>)<sub>3</sub> single crystals ( $x = 0\text{--}1$ ).

single crystals had few defects and impurities. Since the Br contents determined by XPS agree with those determined by SC-XRD as described below, we can justify our XPS sample preparation procedures for enabling us to avoid surface contamination or oxidation which may cause serious errors in the results of surface-sensitive XPS measurement with a detection depth of  $\sim 10$  nm.<sup>24,32</sup>

SC-XRD measurements were performed on 10 single-crystalline samples at 300 K to determine the crystal systems, space groups, lattice parameters, and detailed atomic arrangements. Numerical data obtained for 10 samples are summarized in **Table S3**. We have verified that unit cells of MAPbI<sub>3</sub> ( $x = 0$ ) and MAPbBr<sub>3</sub> ( $x = 1$ ) are tetragonal with *I4/mcm* symmetry and cubic with *Pm̄3m* symmetry, respectively, as previously reported.<sup>33,34</sup> For two samples of low- $x$  MAPb(I<sub>1-x</sub>Br<sub>x</sub>)<sub>3</sub> ( $x = 0.03$  and  $0.06$ ), unit cells were assigned as tetragonal with the space group *I4/mcm* based on observed extinction rules and the validity of the refinement described below. Moreover, for six samples of high- $x$  MAPb(I<sub>1-x</sub>Br<sub>x</sub>)<sub>3</sub> ( $x = 0.08, 0.17, 0.25, 0.50, 0.64$ , and  $0.91$ ), unit cells were unambiguously assigned as cubic with the space group *Pm̄3m*, in clear contrast to the recent argument<sup>35</sup> that  $\alpha$ -phase perovskite crystals exhibit a slightly distorted pseudo-cubic structure. Thus, we can conclude that a boundary between the low- $x$  tetragonal phase and high- $x$  cubic phase exists between  $x = 0.06$  and  $0.08$  at 300 K.

We have accurately determined lattice parameters using the APEX3 program.<sup>36</sup> As summarized in **Table S3**, accuracies of the determined lattice parameters given in Å were better than  $10^{-4}$ . We plotted lattice parameters of MAPb(I<sub>1-x</sub>Br<sub>x</sub>)<sub>3</sub> determined at 300 K as functions of Br content  $x$  determined by XPS in **Figure 3**. For the cubic phase, variation of the lattice parameters is fitted well with a linear relation

$$a_{\text{cubic}} = -0.362x + 6.291 \quad (R = 0.99994) \quad (1)$$

as a function of Br content  $x$ . Meanwhile, variations in the lattice parameters of tetragonal phase are also fitted with linear relations

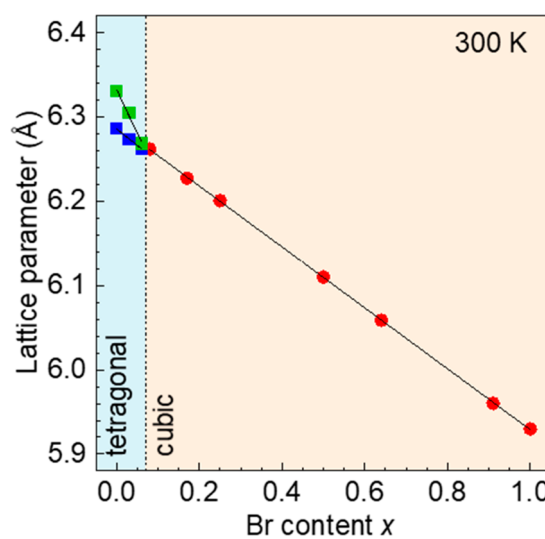


**Figure 3.** Lattice parameters of MAPb(I<sub>1-x</sub>Br<sub>x</sub>)<sub>3</sub> ( $x = 0\text{--}1$ ) at 300 K determined using SC-XRD plotted as functions of Br content  $x$  determined by XPS. Blue squares, green squares, and red circles represent  $a/\sqrt{2}$  in tetragonal phase,  $c/2$  in tetragonal phase, and  $a$  in cubic phase, respectively.

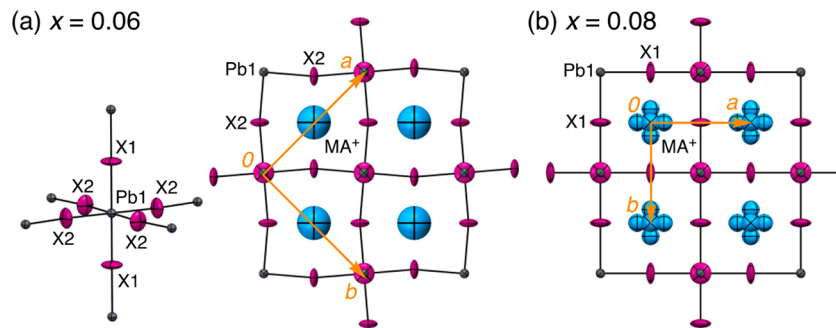


**Figure 4.** Refined atomic arrangements in  $\text{MAPb}(\text{I}_{1-x}\text{Br}_x)_3$ ,  $x = 0.06$  (a) and  $0.08$  (b) viewed along the  $c$  axis. Displacement ellipsoids are drawn at the 50% probability level. Color schemes: Pb, gray; X (Br or I), purple; and  $\text{MA}^+$ , blue.

$$a_{\text{tetragonal}}/\sqrt{2} = -0.394x + 6.286 \quad (R = 0.995) \quad (2)$$

$$c_{\text{tetragonal}}/2 = -1.034x + 6.333 \quad (R = 0.990) \quad (3)$$

Therefore, we can conclude that Vegard's law is strictly valid with accuracy in both phases of  $\text{MAPb}(\text{I}_{1-x}\text{Br}_x)_3$ . (Note that deviations from the linear relations shown in Figure 3 are significantly smaller than those of previous studies summarized in Figure S1.) This result clearly indicates that interactions between  $\text{I}^-$  and  $\text{Br}^-$  anions are negligible and thus that the mixed-halide perovskite  $\text{MAPb}(\text{I}_{1-x}\text{Br}_x)_3$  is a simple random solid solution.

As summarized in Table S3, convergences of atomic-arrangement refinements for all the samples were satisfactorily good suggesting that our samples were of high quality with negligible strains. Additionally, we calculated Br contents based on these crystal structure analyses by refining occupancies of the halide anions ( $\text{I}^-$  and  $\text{Br}^-$ ) on X sites with the total occupancy constrained to unity. Results summarized in Table S3 are in reasonable agreement with the XPS data suggesting the validity of our measurements and analyses. Figure 4 shows refined atomic arrangements of tetragonal  $\text{MAPb}(\text{I}_{1-x}\text{Br}_x)_3$  ( $x = 0.06$ ) and cubic  $\text{MAPb}(\text{I}_{1-x}\text{Br}_x)_3$  ( $x = 0.08$ ) viewed down the  $c$  axis.

**Polycrystalline Thin Films.** We studied seven  $\text{MAPb}(\text{I}_{1-x}\text{Br}_x)_3$  polycrystalline thin films. Lattice parameters of the polycrystalline thin films were determined from 1D WAXS profiles shown in Figure 5 which were obtained by azimuthally integrating 2D WAXS patterns (measured at room temperature (296 K) and shown in Figure S7) by which the influence of crystal orientations can be excluded. We determined the Br contents  $x$  of these  $\text{MAPb}(\text{I}_{1-x}\text{Br}_x)_3$  polycrystalline thin-film samples by substituting  $a_{\text{tetragonal}}$  or  $a_{\text{cubic}}$  obtained from the  $(220)_t$  or  $(200)_c$  peak position in eq 1 or 2. It is quite interesting to compare the accurate Br contents determined by the WAXS measurements with those determined using XPS measurements (Figures S8–S12) performed on the same samples. As shown in Figure 6a,  $x$  values determined by XPS considerably differ from the accurate  $x$  values. Without a doubt, these large errors are caused by the existence of impurities such as  $\text{PbI}_2$  which is evident in 1D WAXS profiles shown in Figure 5. The discrepancy of Br contents obtained from lattice parameters and XPS measurements in Figure 6a is noticeable at  $x = 0.72$ , probably due to the ratio of  $\text{PbI}_2$  to the total iodide anions in the  $\text{MAPb}(\text{I}_{1-x}\text{Br}_x)_3$  polycrystalline thin films. From the present study, we conclude that XPS measurements are not adequate for determining Br/I ratios in  $\text{MAPb}(\text{I}_{1-x}\text{Br}_x)_3$  polycrystalline thin films. Moreover, it

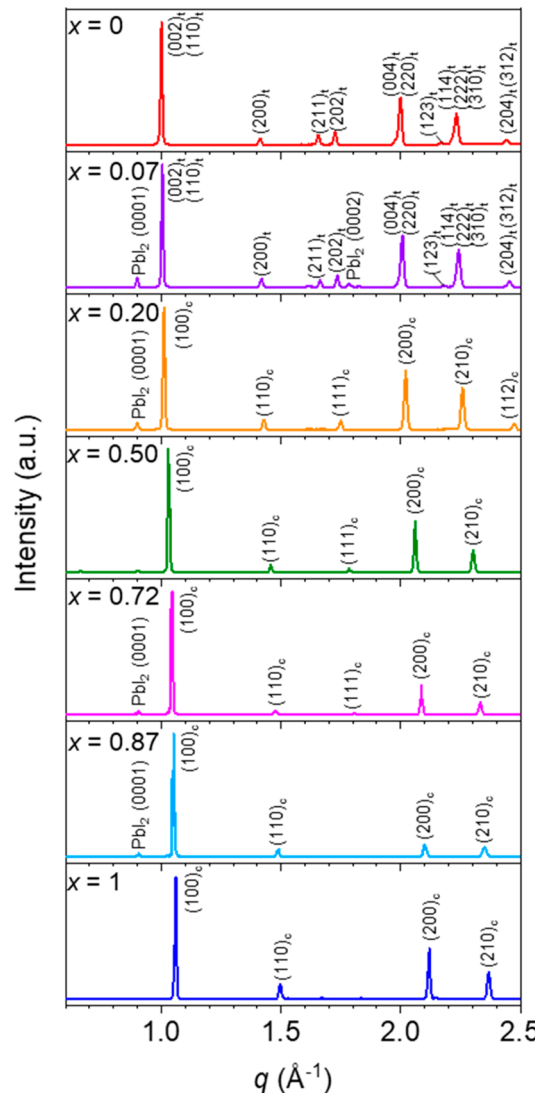


**Figure 5.** 1D WAXS profiles obtained by azimuthally integrating 2D WAXS data (Figure S7) of  $\text{MAPb}(\text{I}_{1-x}\text{Br}_x)_3$  polycrystalline films ( $x = 0$ –1) measured at room temperature (296 K). Br contents  $x$  shown in this figure are determined using the lattice parameters obtained from these profiles.

should be noted that Br contents of polycrystalline thin films are slightly different from those of precursor solutions as shown in Figure 6b even though we used an antisolvent method for preparing polycrystalline thin films which are believed to be a good process suitable for controlling the alloy

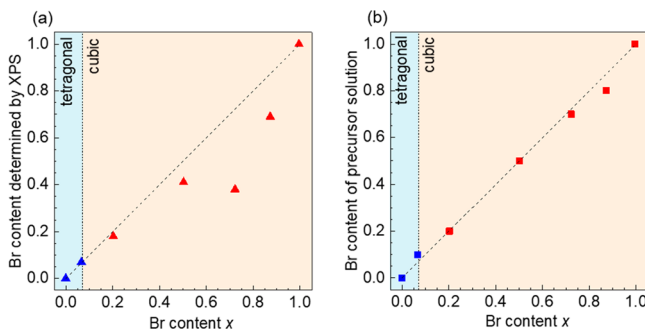


**Figure 6.** (a) Br contents of polycrystalline films measured by XPS and (b) Br contents of precursor solutions versus Br contents of  $\text{MAPb}(\text{I}_{1-x}\text{Br}_x)_3$  polycrystalline films determined by WAXS.

composition. The discrepancy of Br contents is presumably caused by the difference in probability that halide anions are incorporated into the crystal during the crystallization process,<sup>3,37</sup> which is probably governed by the formation of crystal nuclei resulting from complicated processes between solvents and solutes. We conclude that it may be erroneous to determine the Br contents of  $\text{MAPb}(\text{I}_{1-x}\text{Br}_x)_3$  polycrystalline thin-film samples based on precursor solution contents.

We estimated band gap energies of  $\text{MAPb}(\text{I}_{1-x}\text{Br}_x)_3$  using a standard analysis taking into account the excitonic effects<sup>38,39</sup> applied to the absorption spectrum measured using polycrystalline thin-film samples. The measured absorption spectra of  $\text{MAPb}(\text{I}_{1-x}\text{Br}_x)_3$  polycrystalline films (shown in Figures 7 and S13) were fitted with the following equations:

$$\alpha = \int_{-\infty}^{+\infty} [\alpha_{\text{con}}(\hbar\omega - E) + \alpha_{\text{ex}}(\hbar\omega - E)] \exp\left[-\left(\frac{E}{\sqrt{2}\sigma}\right)^2\right] dE \quad (4)$$

$$\alpha_{\text{con}}(\hbar\omega) \propto \frac{2\pi\sqrt{E_b}}{1 - \exp[-2z]} \quad (5)$$

$$\alpha_{\text{ex}}(\hbar\omega) \propto \sum_{n=1}^{\infty} \delta\left(\hbar\omega - \left(E_g - \frac{E_b}{n^2}\right)\right)/n^3 \quad (6)$$

where effects of excitonic absorptions and the Sommerfeld factor with the Gaussian broadening are explicitly included. Here,  $\hbar\omega$  is the photon energy,  $E_g$  is the band gap energy,  $E_b$  is

the exciton binding energy,  $z = \pi \sqrt{\frac{E_b}{\hbar\omega - E_g}}$  is the Sommerfeld factor, and  $n = 1, 2, 3, \dots$  is the quantum number of the exciton series.  $\alpha_{\text{con}}(\hbar\omega)$  and  $\alpha_{\text{ex}}(\hbar\omega)$  are continuum and excitonic contributions, respectively.<sup>40</sup>

The obtained band gap energies and exciton binding energies are plotted as functions of the Br content  $x$  in Figure 8 and Figure S14, respectively. Although band gap energies

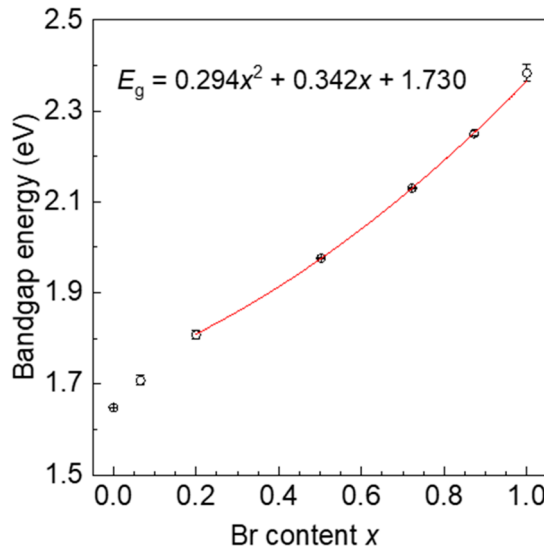


**Figure 8.** Band gap energies of  $\text{MAPb}(\text{I}_{1-x}\text{Br}_x)_3$  determined from absorption spectra of polycrystalline films measured at room temperature (296 K) plotted as a function of Br content  $x$ . The red line represents a quadratic fitting to the band gap energies of cubic phase  $\text{MAPb}(\text{I}_{1-x}\text{Br}_x)_3$ .

increase with increasing Br content as is well-known, we can see a discontinuity between the cubic phase ( $x \geq 0.20$ ) and the tetragonal phase ( $x \leq 0.07$ ). The obtained band gap energies of cubic-phase  $\text{MAPb}(\text{I}_{1-x}\text{Br}_x)_3$  given in eV are well fitted with the following quadratic equation:

$$E_g = 0.294x^2 + 0.342x + 1.730 \quad (7)$$

In addition, the exciton binding energies plotted in Figure S14 increase with increasing Br content  $x$  as reported previously.<sup>41,42</sup> This tendency is natural because lower- $x$  halide

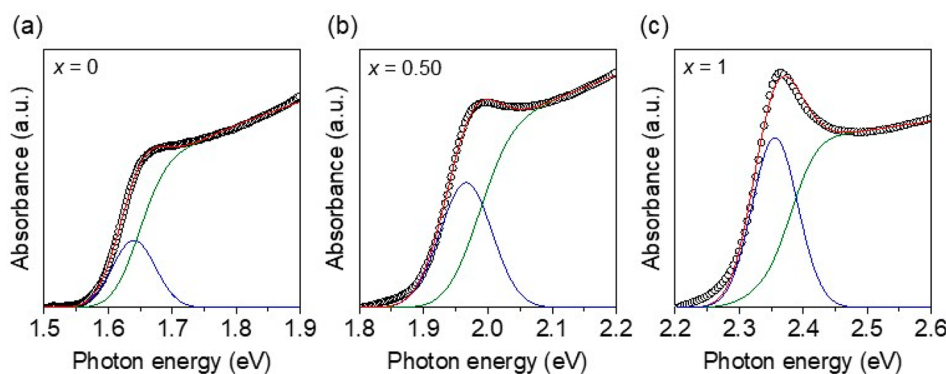


**Figure 7.** Absorption spectra of  $\text{MAPb}(\text{I}_{1-x}\text{Br}_x)_3$  (a)  $x = 0$ , (b)  $x = 0.50$ , and (c)  $x = 1$  polycrystalline films measured at room temperature (296 K). Open circles, red solid lines, blue solid lines, and green solid lines represent experimental data, total absorption, absorption due to excitons, and the continuum absorption due to interband transition, respectively.

perovskites with smaller  $E_g$  exhibit higher dielectric constants that lead to strong dielectric Coulomb screening.

## CONCLUSION

We have precisely determined crystal systems and lattice parameters of mixed-halide perovskite  $\text{MAPb}(\text{I}_{1-x}\text{Br}_x)_3$  as functions of Br content  $x$  using XPS and SC-XRD measurements on single crystalline samples. We conclude that, for  $\text{MAPb}(\text{I}_{1-x}\text{Br}_x)_3$  ( $T = 300$  K),

- (1) For  $x \leq 0.06$ , the crystal system is tetragonal, and the space group is  $I4/mcm$ ; for  $x \geq 0.08$ , the crystal system is cubic, and the space group is  $Pm\bar{3}m$ .
- (2) Lattice parameters are given as functions of  $x$  by eq 1 for the cubic phase and by eqs 2 and 3 for tetragonal phase.

Lattice parameters of  $\text{MAPb}(\text{I}_{1-x}\text{Br}_x)_3$  strictly follow Vegard's law indicating that the mixed-halide perovskite  $\text{MAPb}(\text{I}_{1-x}\text{Br}_x)_3$  is a simple random solid solution with negligible interaction between halide anions. We propose using the equations of  $x$ -dependent lattice parameters obtained in this study for determining Br contents  $x$  of  $\text{MAPb}(\text{I}_{1-x}\text{Br}_x)_3$  samples. Furthermore, we determined band gap energies of  $\text{MAPb}(\text{I}_{1-x}\text{Br}_x)_3$  as a function of the Br content  $x$  taking account of the excitonic effects. The data obtained here are indispensable basic information which can be widely used in crystal engineering and band gap engineering of the mixed-halide perovskite  $\text{MAPb}(\text{I}_{1-x}\text{Br}_x)_3$  for developing high-performance devices, and especially, we believe, for future single-crystal based all-perovskite devices fabricated with the heteroepitaxy<sup>43</sup> technique.

## ASSOCIATED CONTENT

### Supporting Information

The Supporting Information is available free of charge at <https://pubs.acs.org/doi/10.1021/acs.inorgchem.9b03421>.

Previously reported lattice parameters of  $\text{MAPb}(\text{I}_{1-x}\text{Br}_x)_3$ , volumetric ratios of  $\text{MAPbBr}_3/\text{MAPbI}_3$  mixed solutions for growing single crystals, XPS spectra of single crystals, atomic ratios determined by XPS, Br content of single crystals, results of SC-XRD, detailed treatments in SC-XRD analysis, 2D WAXS patterns, XPS spectra of polycrystalline films, absorption spectra, and exciton binding energies ([PDF](#))

### Accession Codes

CCDC 1949354–1949363 contain the supplementary crystallographic data for this paper. These data can be obtained free of charge via [www.ccdc.cam.ac.uk/data\\_request/cif](http://www.ccdc.cam.ac.uk/data_request/cif), or by emailing [data\\_request@ccdc.cam.ac.uk](mailto:data_request@ccdc.cam.ac.uk), or by contacting The Cambridge Crystallographic Data Centre, 12 Union Road, Cambridge CB2 1EZ, UK; fax: +44 1223 336033.

## AUTHOR INFORMATION

### Corresponding Authors

**Naoyuki Shibayama** — Department of General Systems Studies, Graduate School of Arts and Sciences, The University of Tokyo, Tokyo, Japan; [orcid.org/0000-0003-2182-049X](http://orcid.org/0000-0003-2182-049X); Email: [naoyuki.shibayama81@gmail.com](mailto:naoyuki.shibayama81@gmail.com)

**Hiroshi Segawa** — Department of General Systems Studies, Graduate School of Arts and Sciences and Research Center for Advanced Science and Technology, The University of Tokyo, Tokyo, Japan; Email: [csegawa@mail.ecc.u-tokyo.ac.jp](mailto:csegawa@mail.ecc.u-tokyo.ac.jp)

**Takashi Kondo** — Department of Materials Engineering and Research Center for Advanced Science and Technology, The University of Tokyo, Tokyo, Japan; Email: [tkondo@castle.tu-tokyo.ac.jp](mailto:tkondo@castle.tu-tokyo.ac.jp)

### Authors

**Yuiga Nakamura** — Department of Materials Engineering, The University of Tokyo, Tokyo, Japan

**Akiko Hori** — Graduate School of Engineering and Science, Shibaura Institute of Technology, Saitama, Japan

**Tomonori Matsushita** — Department of Materials Engineering and Research Center for Advanced Science and Technology, The University of Tokyo, Tokyo, Japan

Complete contact information is available at: <https://pubs.acs.org/10.1021/acs.inorgchem.9b03421>

### Author Contributions

Y.N. performed all experiments and wrote the manuscript. N.S. and T.K. provided Y.N. with research instruction as well as assisted in writing the manuscript and the experiments. A.H. performed SC-XRD analysis. T.M. carried out the discussion. H.S. and T.K. supervised the project. All authors contributed to discussions and to finalizing the manuscript.

### Notes

The authors declare no competing financial interest.

## ACKNOWLEDGMENTS

This work was supported by New energy and industrial Technology Development Organization (NEDO), Japan. The authors thank Dr. Fujiwara, and Dr. Koganezawa from Japan Synchrotron Radiation Research Institute (JASRI) and Dr. Yoza, Dr. Morioka, and Dr. Yamada from Bruker Japan K. K. for discussions. The 2D WAXS measurements were performed at SPring-8 with the approval of the JASRI (Proposal Nos. 2018B1862, 2019A1708, 2019A1774, 2019A1829, 2019B1807, 2019B1808, and 2019B2017). Part of this work was supported by Nanotechnology Platform (Project No. A-18-UT-0171, 19008316, 18008135) of the Ministry of Education, Culture, Sports, Science and Technology (MEXT), Japan.

## REFERENCES

- (1) Kojima, A.; Teshima, K.; Shirai, Y.; Miyasaka, T. Organometal Halide Perovskites as Visible-Light Sensitizers for Photovoltaic Cells. *J. Am. Chem. Soc.* **2009**, *131*, 6050–6051.
- (2) <http://www.nrel.gov/pv/assets/pdfs/best-research-cell-efficiencies.20190802.pdf>.
- (3) Dunlap-Shohl, W. A.; Zhou, Y.; Padture, N. P.; Mitzi, D. B. Synthetic Approaches for Halide Perovskite Thin Films. *Chem. Rev.* **2019**, *119*, 3193–3295.
- (4) Chun, D. H.; Choi, Y. J.; In, Y.; Nam, J. K.; Choi, Y. J.; Yun, S.; Kim, W.; Choi, D.; Kim, D.; Shin, H.; Cho, J. H.; Park, J. H. Halide perovskite nanopillar photodetector. *ACS Nano* **2018**, *12*, 8564–8571.
- (5) Chen, Y.-J.; Li, M.-H.; Liu, J.-Y.; Chong, C.-W.; Huang, J.-C.; Chen, P. Double-side operable perovskite photodetector using Cu/Cu<sub>2</sub>O as a hole transport layer. *Opt. Express* **2019**, *27*, 24900–24913.
- (6) Daus, A.; Roldan-Carmona, C.; Domanski, K.; Knobelspies, S.; Cantarella, G.; Vogt, C.; Graetzel, M.; Nazeeruddin, M. K.; Troester, G. Metal-Halide Perovskites for Gate Dielectrics in Field-Effect Transistors and Photodetectors Enabled by PMMA Lift-Off Process. *Adv. Mater.* **2018**, *30*, 1707412.
- (7) Lin, K.; Xing, J.; Quan, L. N.; de Arquer, F. P. G.; Gong, X.; Lu, J.; Xie, L.; Zhao, W.; Zhang, D.; Yan, C.; Li, W.; Liu, X.; Lu, Y.; Kirman, J.; Sargent, E. H.; Xiong, Q.; Wei, Z. Perovskite light-emitting

- diodes with external quantum efficiency exceeding 20%. *Nature* **2018**, *S62*, 245–248.
- (8) Li, Z.; Moon, J.; Gharajeh, A.; Haroldson, R.; Hawkins, R.; Hu, W.; Zakhidov, A.; Gu, Q. Room-Temperature Continuous-Wave Operation of Organometal Halide Perovskite Lasers. *ACS Nano* **2018**, *12*, 10968–10976.
- (9) Miyasaka, T. Lead Halide Perovskites in Thin Film Photovoltaics: Background and Perspectives. *Bull. Chem. Soc. Jpn.* **2018**, *91*, 1058–1068.
- (10) Seok, S. I.; Graetzel, M.; Park, N.-G. Methodologies toward Highly Efficient Perovskite Solar Cells. *Small* **2018**, *14*, 1704177.
- (11) Charles, B.; Dillon, J.; Weber, O. J.; Islam, M. S.; Weller, M. T. Understanding the stability of mixed A-cation lead iodide perovskites. *J. Mater. Chem. A* **2017**, *5*, 22495–22499.
- (12) Gratia, P.; Zimmermann, I.; Schouwink, P.; Yum, J.-H.; Audinot, J.-N.; Sivula, K.; Wirtz, T.; Nazeeruddin, M. K. The Many Faces of Mixed Ion Perovskites: Unraveling and Understanding the Crystallization Process. *ACS Energy Lett.* **2017**, *2*, 2686–2693.
- (13) Reyna, Y.; Salado, M.; Kazim, S.; Pérez-Tomas, A.; Ahmad, S.; Lira-Cantu, M. Performance and stability of mixed (FAPbI<sub>3</sub>)<sub>0.85</sub>(MAPbBr<sub>3</sub>)<sub>0.15</sub> halide perovskite solar cells under outdoor conditions and the effect of low light irradiation. *Nano Energy* **2016**, *30*, 570–579.
- (14) Pazoki, M.; Edvinsson, T. Nature of the excited state in lead iodide perovskite materials: Time-dependent charge density response and the role of the monovalent cation. *Phys. Rev. B: Condens. Matter Mater. Phys.* **2019**, *100*, 045203.
- (15) Jacobsson, T. J.; Correa-Baena, J.-P.; Pazoki, M.; Saliba, M.; Schenk, K.; Graetzel, M.; Hagfeldt, A. Exploration of the compositional space for mixed lead halogen perovskites for high efficiency solar cells. *Energy Environ. Sci.* **2016**, *9*, 1706–1724.
- (16) Noh, J. H.; Im, S. H.; Heo, J. H.; Mandal, T. N.; Seok, S. I. Chemical management for colorful, efficient, and stable inorganic-organic hybrid nanostructured solar cells. *Nano Lett.* **2013**, *13*, 1764–1769.
- (17) Kulkarni, S. A.; Baikie, T.; Boix, P. P.; Yantara, N.; Mathews, N.; Mhaisalkar, S. Band-gap tuning of lead halide perovskites using a sequential deposition process. *J. Mater. Chem. A* **2014**, *2*, 9221–9225.
- (18) Fedeli, P.; Gazza, F.; Calestani, D.; Ferro, P.; Besagni, T.; Zappettini, A.; Calestani, G.; Marchi, E.; Ceroni, P.; Mosca, R. Influence of the Synthetic Procedures on the Structural and Optical Properties of Mixed-Halide (Br, I) Perovskite Films. *J. Phys. Chem. C* **2015**, *119*, 21304–21313.
- (19) Sadhanala, A.; Deschler, F.; Thomas, T. H.; Dutton, S. E.; Goedel, F. C.; Hanusch, F. C.; Lai, M. L.; Steiner, U.; Bein, T.; Docampo, P.; Cahen, D.; Friend, R. H. Preparation of Single-Phase Films of CH<sub>3</sub>NH<sub>3</sub>Pb(I<sub>1-x</sub>Br<sub>x</sub>)<sub>3</sub> with Sharp Optical Band Edges. *J. Phys. Chem. Lett.* **2014**, *5*, 2501–2505.
- (20) Atourki, L.; Vega, E.; Marí, B.; Mollar, M.; Ahsaine, H. A.; Bouabid, K.; Ihlal, A. Role of the chemical substitution on the structural and luminescence properties of the mixed halide perovskite thin MAPbI<sub>3-x</sub>Br<sub>x</sub> (0 ≤ x ≤ 1) films. *Appl. Surf. Sci.* **2016**, *371*, 112–117.
- (21) Misra, R. K.; Ciammaruchi, L.; Aharon, S.; Mogilyansky, D.; Etgar, L.; Visoly-Fisher, I.; Katz, E. A. Effect of Halide Composition on the Photochemical Stability of Perovskite Photovoltaic Materials. *ChemSusChem* **2016**, *9*, 2572–2577.
- (22) Zhang, Y.; Liu, Y.; Li, Y.; Yang, Z.; Liu, S. Perovskite CH<sub>3</sub>NH<sub>3</sub>Pb(Br<sub>x</sub>I<sub>1-x</sub>)<sub>3</sub> single crystals with controlled composition for fine-tuned bandgap towards optimized optoelectronic applications. *J. Mater. Chem. C* **2016**, *4*, 9172–9178.
- (23) Wang, W.; Su, J.; Zhang, L.; Lei, Y.; Wang, D.; Lu, D.; Bai, Y. Growth of mixed-halide perovskite single crystals. *CrystEngComm* **2018**, *20*, 1635–1643.
- (24) Philippe, B.; Jacobsson, T. J.; Correa-Baena, J.-P.; Jena, N. K.; Banerjee, A.; Chakraborty, S.; Cappel, U. B.; Ahuja, R.; Hagfeldt, A.; Odelius, M.; Rensmo, H. Valence Level Character in a Mixed Perovskite Material and Determination of the Valence Band Maximum from Photoelectron Spectroscopy: Variation with Photon Energy. *J. Phys. Chem. C* **2017**, *121*, 26655–26666.
- (25) Castellanos, M.; West, A. R. Deviations from Vegard's law in oxide solid solutions. The systems Li<sub>2</sub>TiO<sub>3</sub>-MgO and Li<sub>2</sub>TiO<sub>3</sub>-Na<sub>2</sub>TiO<sub>3</sub>. *J. Chem. Soc., Faraday Trans. 1* **1980**, *76*, 2159–2169.
- (26) Shibayama, N.; Fukumoto, S.; Sugita, H.; Kanda, H.; Ito, S. Influence of transparent conductive oxide layer on the inverted perovskite solar cell using PEDOT: PSS for hole transport layer. *Mater. Res. Bull.* **2018**, *106*, 433–438.
- (27) Kanda, H.; Shibayama, N.; Uzum, A.; Umeyama, T.; Imahori, H.; Ibi, K.; Ito, S. Effect of Silicon Surface for Perovskite/Silicon Tandem Solar Cells: Flat or Textured? *ACS Appl. Mater. Interfaces* **2018**, *10*, 35016–35024.
- (28) Sheldrick, G. M. SHELXT - Integrated space-group and crystal-structure determination. *Acta Crystallogr., Sect. A: Found. Adv.* **2015**, *A71*, 3–8.
- (29) Sheldrick, G. M. Crystal structure refinement with SHELXL. *Acta Crystallogr., Sect. C: Struct. Chem.* **2015**, *C71*, 3–8.
- (30) Shibayama, N.; Kanda, H.; Kim, T. W.; Segawa, H.; Ito, S. Design of BCP buffer layer for inverted perovskite solar cells using ideal factor. *APL Mater.* **2019**, *7*, 031117.
- (31) Zhang, Y.; Huang, F.; Mi, Q. Preferential Facet Growth of Methylammonium Lead Halide Single Crystals Promoted by Halide Coordination. *Chem. Lett.* **2016**, *45*, 1030–1032.
- (32) Kanda, H.; Shibayama, N.; Huckaba, A. J.; Lee, Y.; Paek, S.; Klipfel, N.; Roldán-Carmona, C.; Queloz, V. I. E.; Grancini, G.; Zhang, Y.; Abuhelaiqa, M.; Cho, K. T.; Li, M.; Mensi, M. D.; Kinge, S.; Nazeeruddin, M. K. Band-bending induced passivation: high performance and stable perovskite solar cells using a perhydropoly(silazane) precursor. *Energy Environ. Sci.* **2020**, in press. DOI: 10.1039/C9EE02028D.
- (33) Poglitsch, A.; Weber, D. Dynamic disorder in methylammoniumtrihalogenoplumbates (II) observed by millimeter-wave spectroscopy. *J. Chem. Phys.* **1987**, *87*, 6373–6378.
- (34) Baikie, T.; Fang, Y.; Kadro, J. M.; Schreyer, M.; Wei, F.; Mhaisalkar, S. G.; Graetzel, M.; White, T. J. Synthesis and crystal chemistry of the hybrid perovskite (CH<sub>3</sub>NH<sub>3</sub>)PbI<sub>3</sub> for solid-state sensitised solar cell applications. *J. Mater. Chem. A* **2013**, *1*, 5628–5641.
- (35) Green, M. A.; Ho-Baillie, A.; Snaith, H. J. The emergence of perovskite solar cells. *Nat. Photonics* **2014**, *8*, 506–514.
- (36) APEX3, SAINT and SADABS; Bruker AXS Inc.: Madison, Wisconsin, USA, 2017.
- (37) Hu, H.; Singh, M.; Wan, X.; Tang, J.; Chu, C.-W.; Li, G. Nucleation and crystal growth control for scalable solution-processed organic-inorganic hybrid perovskite solar cells. *J. Mater. Chem. A* **2020**, *8*, 1578–1603.
- (38) Yamada, Y.; Nakamura, T.; Endo, M.; Wakamiya, A.; Kanemitsu, Y. Photoelectronic responses in solution-processed perovskite CH<sub>3</sub>NH<sub>3</sub>PbI<sub>3</sub> solar cells studied by photoluminescence and photoabsorption spectroscopy. *IEEE J. Photovolt.* **2015**, *5*, 401–405.
- (39) Ruf, F.; Aygünler, M. F.; Giesbrecht, N.; Rendenbach, B.; Magin, A.; Docampo, P.; Kalt, H.; Hetterich, M. Temperature-dependent studies of exciton binding energy and phase-transition suppression in (Cs, FA, MA)Pb(I, Br)<sub>3</sub> perovskites. *APL Mater.* **2019**, *7*, 031113.
- (40) Basu, P. K. *The theory of optical processes in semiconductors*; Clarendon Press: Oxford, 1997.
- (41) Miyata, A.; Mitioglu, A.; Plochocka, P.; Portugall, O.; Wang, J. T.-W.; Stranks, S. D.; Snaith, H. J.; Nicholas, R. J. Direct Measurement of the Exciton Binding Energy and Effective Masses for Charge carriers in an Organic-Inorganic Tri-halide Perovskite. *Nat. Phys.* **2015**, *11*, 582–587.
- (42) Galkowski, K.; Mitioglu, A.; Miyata, A.; Plochocka, P.; Portugall, O.; Eperon, G. E.; Wang, J. T.-W.; Stergiopoulos, T.; Stranks, S. D.; Snaith, H. J.; Nicholas, R. J. Determination of the exciton binding energy and effective masses for methylammonium and formamidinium lead tri-halide perovskite semiconductors. *Energy Environ. Sci.* **2016**, *9*, 962–970.

(43) Kimura, K.; Nakamura, Y.; Matsushita, T.; Kondo, T. Epitaxial  $\text{CH}_3\text{NH}_3\text{Pb}(\text{Br}_{1-x}\text{I}_x)_3$  thin films on  $\text{CH}_3\text{NH}_3\text{PbBr}_3$  single crystal substrates formed by physical vapor deposition. *Jpn. J. Appl. Phys.* 2019, 58, SBBF04.

## Supporting Information

# Crystal Systems and Lattice Parameters of $\text{CH}_3\text{NH}_3\text{Pb}(\text{I}_{1-x}\text{Br}_x)_3$ Determined Using Single Crystals: Validity of Vegard's Law

Yuiga Nakamura<sup>1</sup>, Naoyuki Shibayama<sup>2\*</sup>, Akiko Hori<sup>3</sup>,  
Tomonori Matsushita<sup>1,4</sup>, Hiroshi Segawa<sup>2,4\*</sup>, Takashi Kondo<sup>1,4\*</sup>

1. Department of Materials Engineering, The University of Tokyo, Tokyo, Japan
2. Department of General Systems Studies, Graduate School of Arts and Sciences, The University of Tokyo, Tokyo, Japan
3. Graduate School of Engineering and Science, Shibaura Institute of Technology, Saitama, Japan
4. Research Center for Advanced Science and Technology, The University of Tokyo, Tokyo, Japan

Corresponding to: naoyuki.shibayama81@gmail.com (Naoyuki Shibayama)

csegawa@mail.ecc.u-tokyo.ac.jp (Hiroshi Segawa)

tkondo@castle.t.u-tokyo.ac.jp (Takashi Kondo)

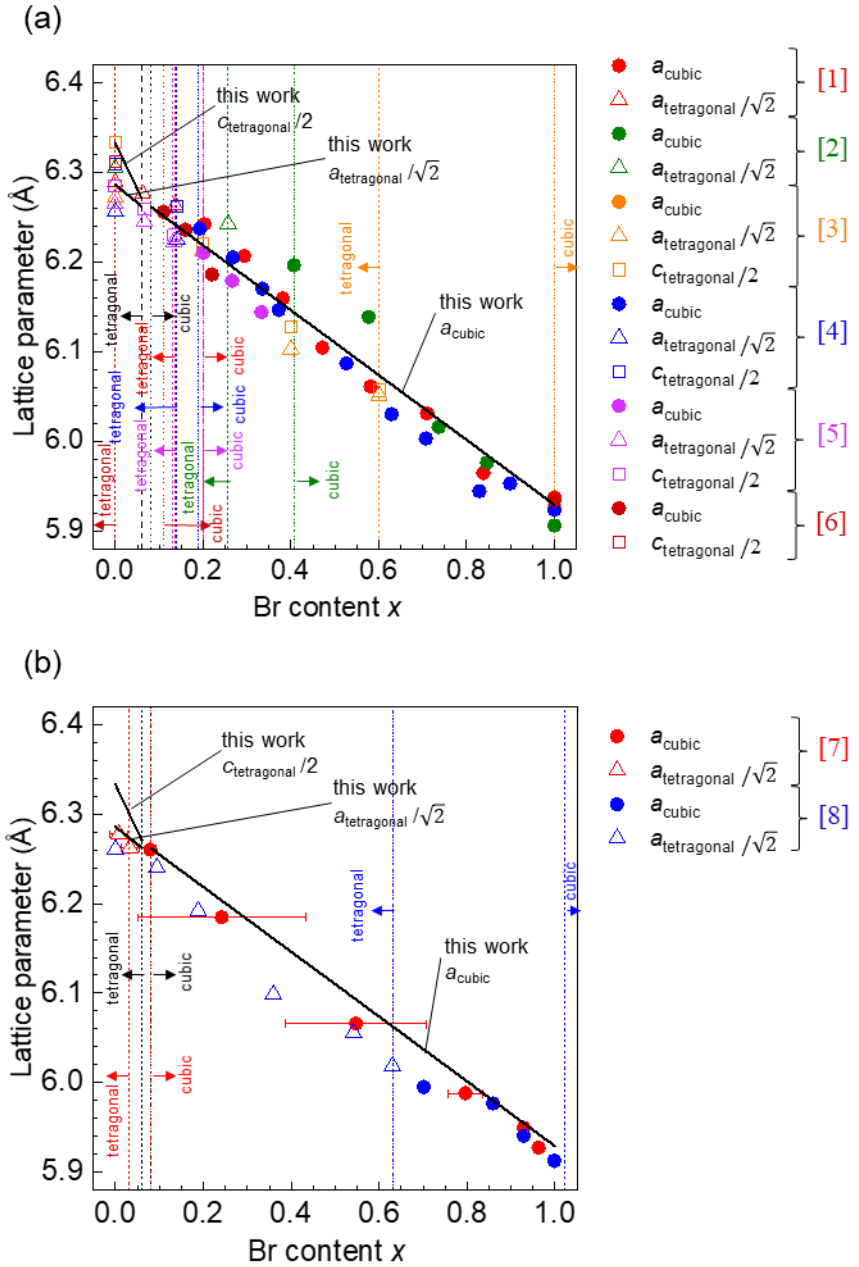


Figure S1. Summary of previously reported lattice parameters of  $\text{MAPb}(\text{I}_{1-x}\text{Br}_x)_3$  as functions of Br content  $x$ . (a) Data obtained using polycrystalline films, (b) data obtained using powder samples. Boundaries between tetragonal and cubic phases are also shown. Black solid lines represent  $x$ -dependent lattice parameters determined in the present study.

Table S1. The volumetric ratios of MAPbBr<sub>3</sub>/MAPbI<sub>3</sub> mixed solutions used for growing MAPb(I<sub>1-x</sub>Br<sub>x</sub>)<sub>3</sub> single crystals.

| Single crystal sample number | Br content obtained from XPS | MAPbBr <sub>3</sub><br>(0.7 M)<br>Volume (mL) | MAPbI <sub>3</sub><br>(1.3 M)<br>Volume (mL) |
|------------------------------|------------------------------|---|--|
| A                            | 0                            | 0   | 6.000  |
| B                            | 0.03                         | 0.3167  | 5.684  |
| C                            | 0.06                         | 0.5190  | 5.481  |
| D                            | 0.08                         | 0.8150  | 5.185  |
| E                            | 0.17                         | 1.005   | 4.995  |
| F                            | 0.25                         | 1.886   | 4.114  |
| G                            | 0.50                         | 2.796   | 3.204  |
| H                            | 0.64                         | 3.325   | 2.675  |
| I                            | 0.91                         | 4.424   | 1.576  |
| J                            | 1                            | 6.000   | 0  |

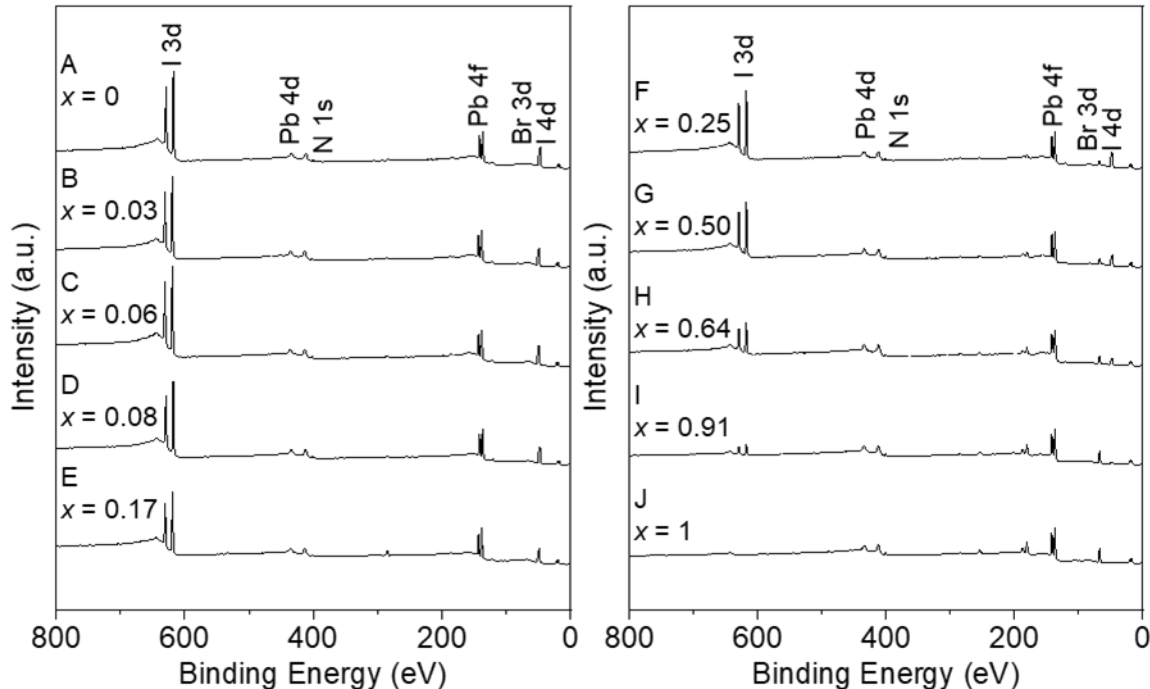


Figure S2. Survey XPS spectra of MAPb(I<sub>1-x</sub>Br<sub>x</sub>)<sub>3</sub> single crystals ( $x = 0\text{--}1$ ).

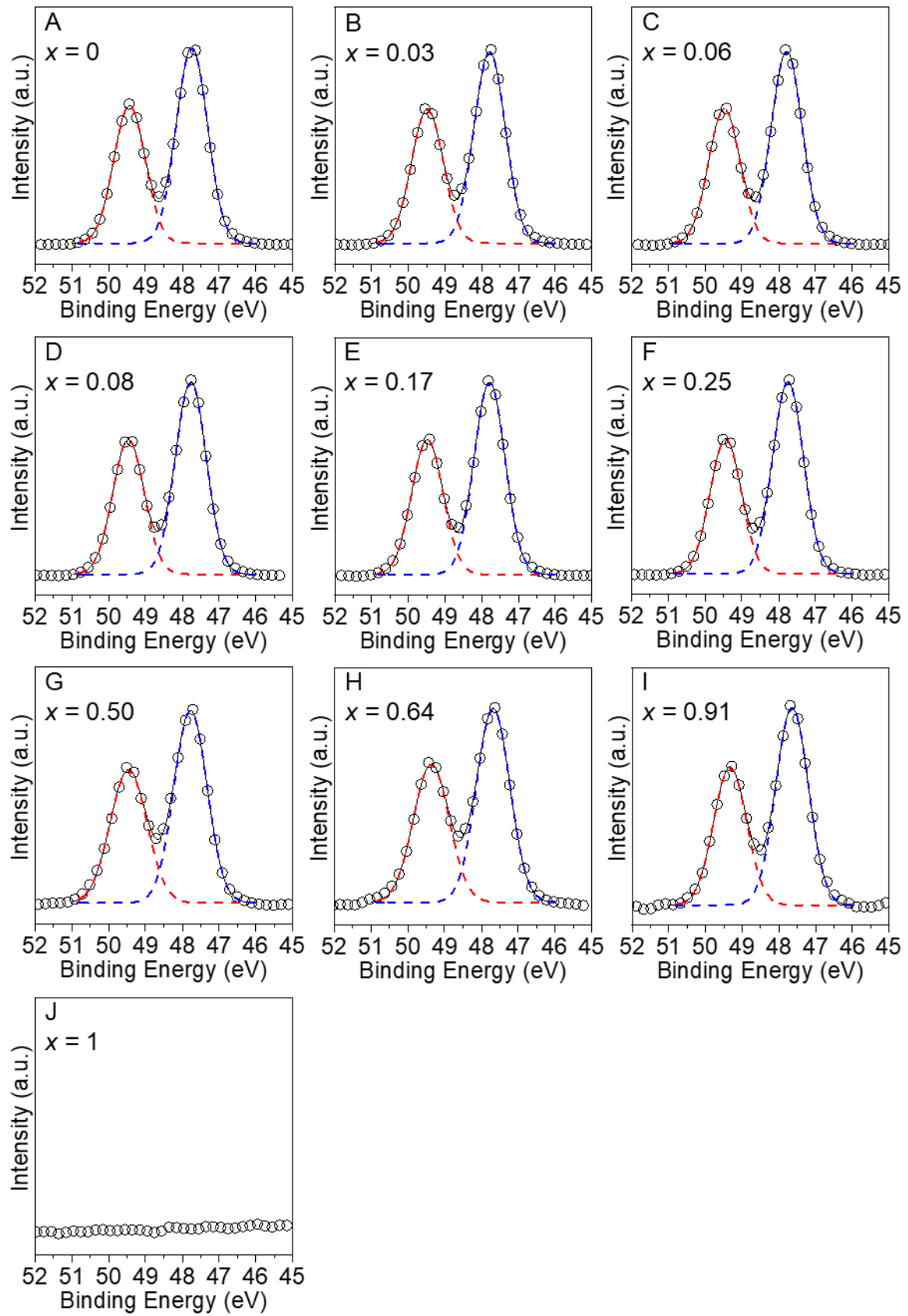


Figure S3. I 4d XPS spectra of MAPb(I<sub>1-x</sub>Br<sub>x</sub>)<sub>3</sub> single crystals ( $x = 0\text{--}1$ ).

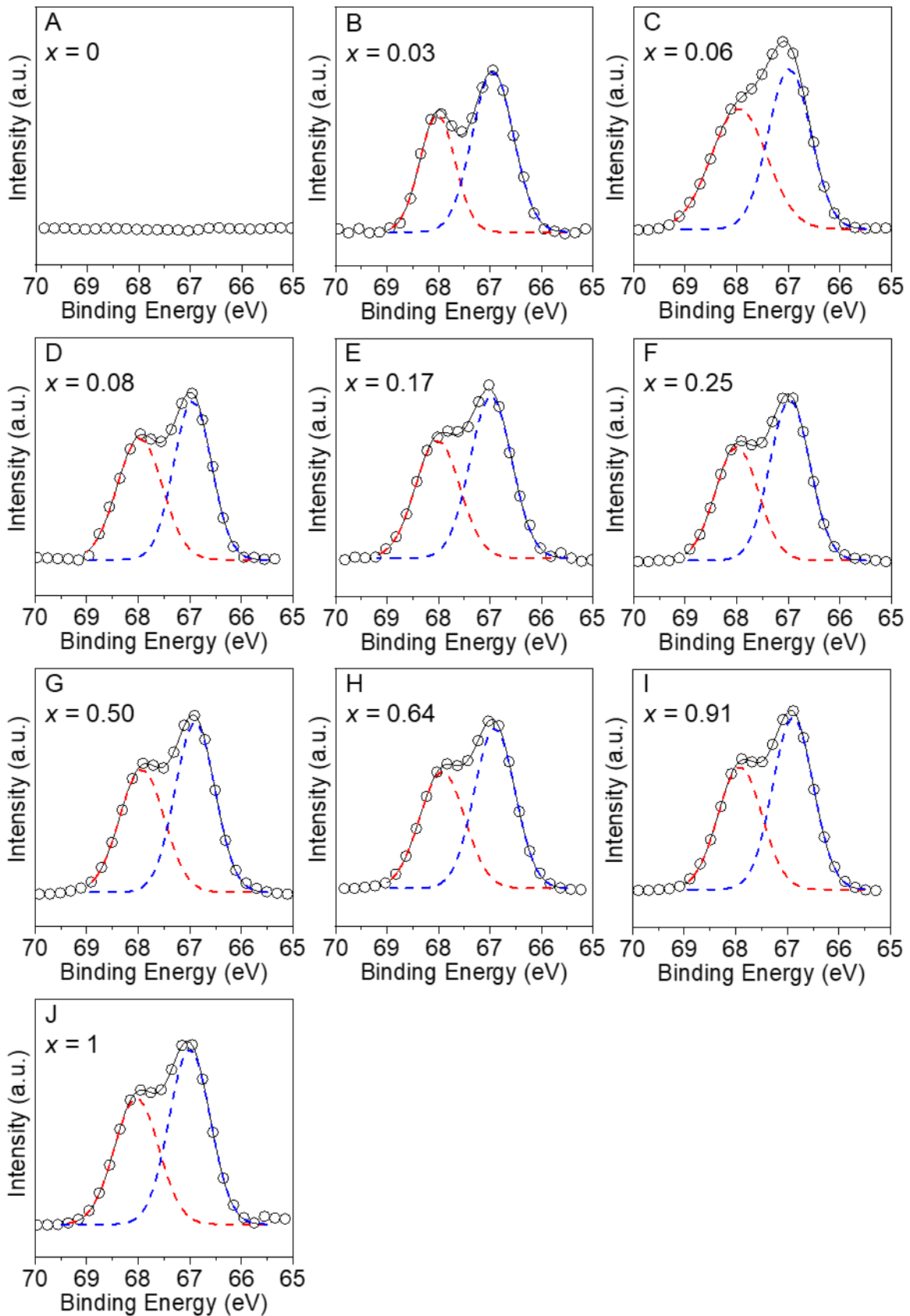


Figure S4. Br 3d XPS spectra of MAPb(I<sub>1-x</sub>Br<sub>x</sub>)<sub>3</sub> single crystals ( $x = 0\text{--}1$ ).

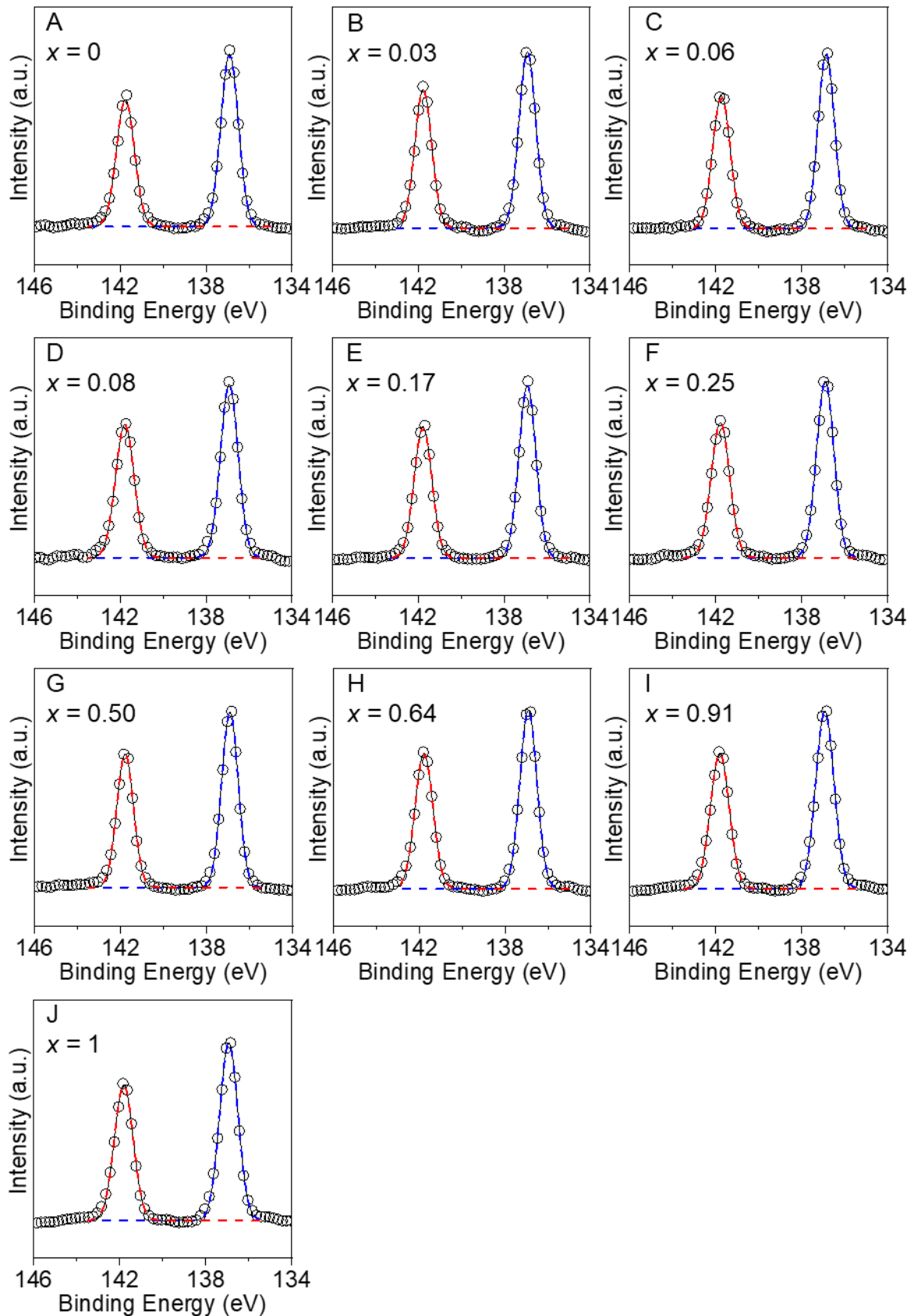


Figure S5. Pb 4f XPS spectra of MAPb(I<sub>1-x</sub>Br<sub>x</sub>)<sub>3</sub> single crystals (*x* = 0–1).

Table S2. The atomic ratios in MAPb(I<sub>1-x</sub>Br<sub>x</sub>)<sub>3</sub> single-crystalline samples determined by XPS

|                            | A    | B    | C    | D    | E    | F    | G    | H    | I    | J    |
|----------------------------|------|------|------|------|------|------|------|------|------|------|
| Pb                         | 0.25 | 0.25 | 0.25 | 0.25 | 0.25 | 0.25 | 0.25 | 0.25 | 0.25 | 0.25 |
| I                          | 0.75 | 0.73 | 0.71 | 0.69 | 0.62 | 0.57 | 0.38 | 0.27 | 0.07 | 0.00 |
| Br                         | 0.00 | 0.02 | 0.04 | 0.06 | 0.13 | 0.19 | 0.37 | 0.48 | 0.68 | 0.75 |
| (I + Br)/Pb                | 3.00 | 3.01 | 3.00 | 3.00 | 3.00 | 3.01 | 2.99 | 3.00 | 2.99 | 3.00 |
| Br content<br>( <i>x</i> ) | 0.00 | 0.03 | 0.06 | 0.08 | 0.17 | 0.25 | 0.50 | 0.64 | 0.91 | 1.00 |

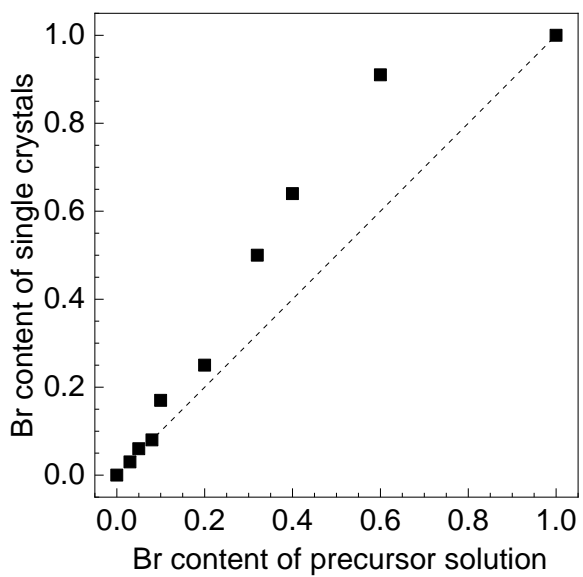


Figure S6. Br content  $x$  of  $\text{MAPb}(\text{I}_{1-x}\text{Br}_x)_3$  single crystals ( $x = 0\text{--}1$ ) determined by XPS versus Br content  $\text{MAPbI}_3/\text{MAPbBr}_3$  solutions used for growing single crystals.

Table S3. Results of SC-XRD of single-crystal  $\text{MAPb}(\text{I}_{1-x}\text{Br}_x)_3$ .

| Sample name                    | A              | B              | C              | D             | E             | F             | G             | H             | I             | J             |
|--------------------------------|----------------|----------------|----------------|---------------|---------------|---------------|---------------|---------------|---------------|---------------|
| Br content (XPS)               | 0              | 0.03           | 0.06           | 0.08          | 0.17          | 0.25          | 0.50          | 0.64          | 0.91          | 1             |
| Br content (SC-XRD)            | 0              | 0.01(6)        | 0.04(4)        | 0.04(3)       | 0.17(3)       | 0.24(4)       | 0.49(2)       | 0.638(12)     | 0.857(14)     | 1             |
| Crystal system                 | tetragonal     | tetragonal     | tetragonal     | cubic         |
| Space group                    | <i>I</i> 4/mcm | <i>I</i> 4/mcm | <i>I</i> 4/mcm | <i>P</i> m-3m |
| <i>a</i> [Å]                   | 8.8907(5)      | 8.8720(4)      | 8.8573(2)      | 6.2623(2)     | 6.2275(3)     | 6.201(2)      | 6.1101(4)     | 6.0588(3)     | 5.9603(4)     | 5.9298(2)     |
| <i>b</i> [Å]                   | 8.8907(5)      | 8.8720(4)      | 8.8573(2)      | 6.2623(2)     | 6.2275(3)     | 6.201(2)      | 6.1101(4)     | 6.0588(3)     | 5.9603(4)     | 5.9298(2)     |
| <i>c</i> [Å]                   | 12.6618(7)     | 12.6105(6)     | 12.5377(3)     | 6.2623(2)     | 6.2275(3)     | 6.201(2)      | 6.1101(4)     | 6.0588(3)     | 5.9603(4)     | 5.9298(2)     |
| <i>V</i> [Å <sup>3</sup> ]     | 1000.85(13)    | 992.60(10)     | 983.60(5)      | 245.58(2)     | 241.51(3)     | 238.4(2)      | 228.11(4)     | 222.41(3)     | 211.74(4)     | 208.51(2)     |
| <i>Z</i>                       | 4              | 4              | 4              | 1             | 1             | 1             | 1             | 1             | 1             | 1             |
| <i>F</i> (000)                 | 1040           | 968            | 968            | 242           | 242           | 242           | 242           | 224           | 224           | 206           |
| <i>R</i> <sub>int</sub>        | 0.0773         | 0.0744         | 0.0865         | 0.0493        | 0.0715        | 0.0994        | 0.0669        | 0.0455        | 0.0605        | 0.1195        |
| Reflections measured           | 4670           | 4723           | 4712           | 2547          | 2687          | 1975          | 2380          | 2486          | 2422          | 3485          |
| Reflections independent        | 259            | 257            | 254            | 68            | 68            | 68            | 63            | 63            | 60            | 57            |
| <i>R</i> [ $(I) > 2s(I)$ ]     | 0.0566         | 0.0722         | 0.0573         | 0.0375        | 0.022         | 0.0334        | 0.0176        | 0.0106        | 0.0108        | 0.0102        |
| <i>wR</i> ( $F_{\text{o}}^2$ ) | 0.1241         | 0.1757         | 0.1447         | 0.0812        | 0.0502        | 0.0761        | 0.0428        | 0.0248        | 0.0267        | 0.0235        |
| GOF                            | 1.259          | 1.341          | 1.549          | 1.385         | 1.219         | 1.49          | 1.173         | 1.286         | 1.225         | 1.256         |
| CCDC No.                       | 1949354        | 1949355        | 1949356        | 1949357       | 1949358       | 1949359       | 1949360       | 1949361       | 1949362       | 1949363       |

## Detailed treatment of disorder atoms in SC-XRD analysis

The refinements for disorder atoms, Br and I, were performed using general method with EXYZ command, which the same  $x$ ,  $y$  and  $z$  parameters are used for Br and I. This is general and useful method when atoms of different elements share the same site, in which case EADP command, the same isotropic or anisotropic displacement parameters, also used with EXYZ.

## Detailed treatment of $\text{MA}^+$ in SC-XRD analysis

The electron density of the cation component ( $\text{MA}^+$ ) could not be obtained as a three-dimensional molecular structure in the crystal at 300 K because of the free rotation of  $\text{MA}^+$  (Fig. 4), which was previously observed using neutron diffraction measurements.<sup>9</sup> Therefore, after refining the structure of the Pb, I, and Br frameworks, the MA component (C, H, and N) was placed on one appropriate residual peak appearing as the difference in the Fourier synthesis in the voids of the frameworks to provide the analytical structure with good validity. It is consistent with previous works to assume that the arrangement of  $\text{MA}^+$  in the cubic structure has a cubic symmetry rather than a spherical symmetry.<sup>10,11</sup>

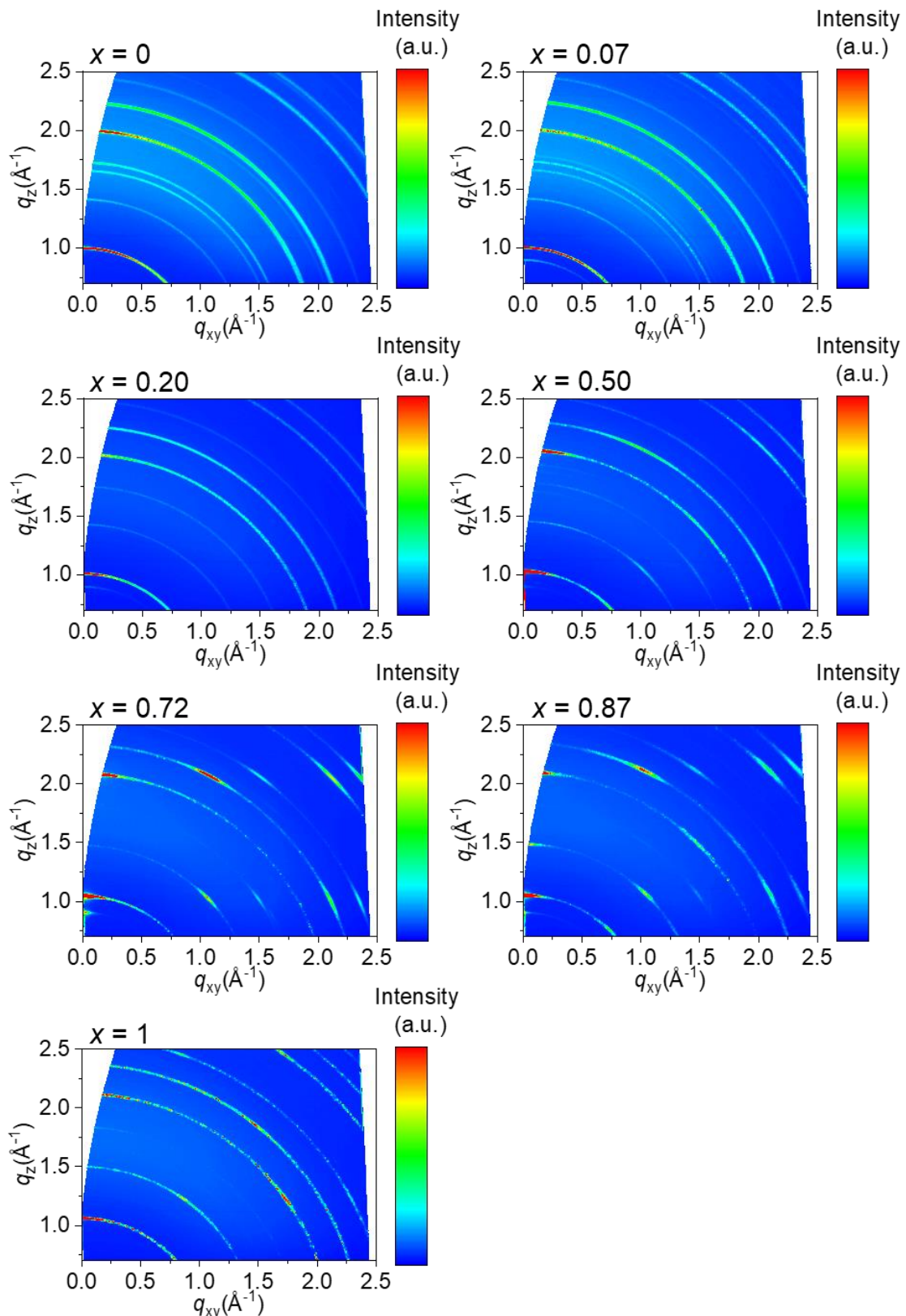


Figure S7. 2D WAXS patterns of the MAPb(I<sub>1-x</sub>Br<sub>x</sub>)<sub>3</sub> polycrystalline films measured at room temperature (296 K) (a)  $x = 0$ , (b)  $x = 0.07$ , (c)  $x = 0.20$ , (d)  $x = 0.50$ , (e)  $x = 0.72$ , (f)  $x = 0.87$ , and (g)  $x = 1$ .

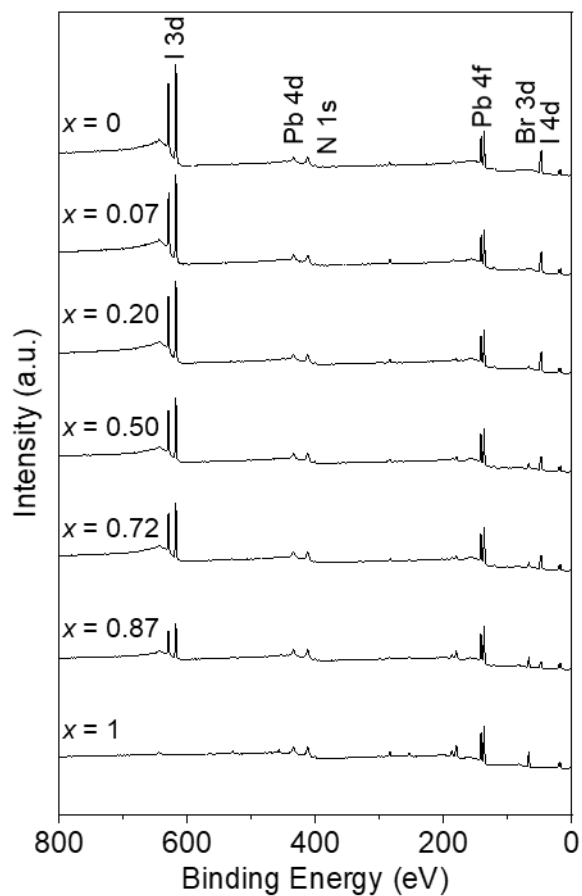


Figure S8. Survey XPS spectra of  $\text{MAPb}(\text{I}_{1-x}\text{Br}_x)_3$  polycrystalline films ( $x = 0\text{--}1$ ).

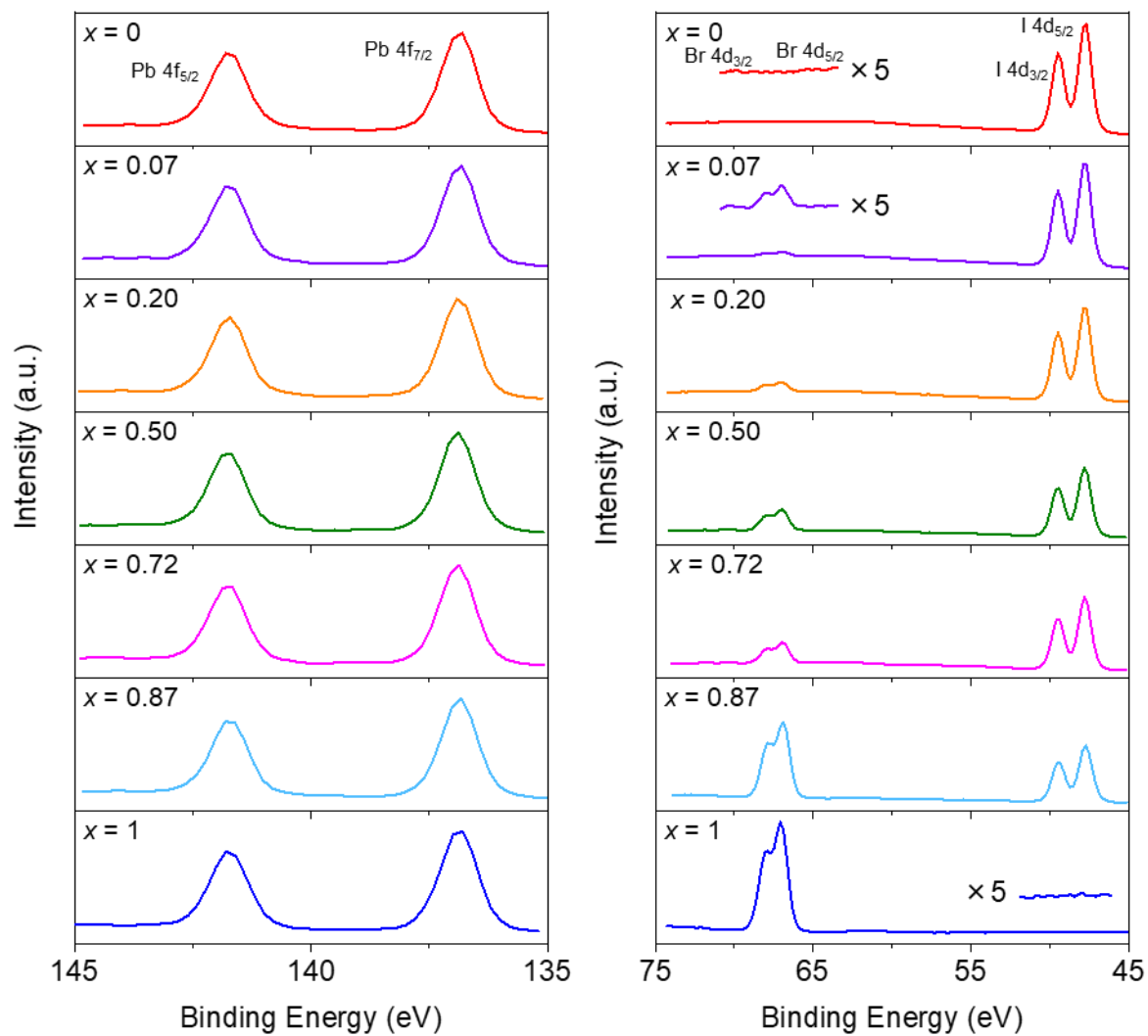


Figure S9. XPS spectra of MAPb(I<sub>1-x</sub>Br<sub>x</sub>)<sub>3</sub> polycrystalline films ( $x = 0\text{--}1$ ).

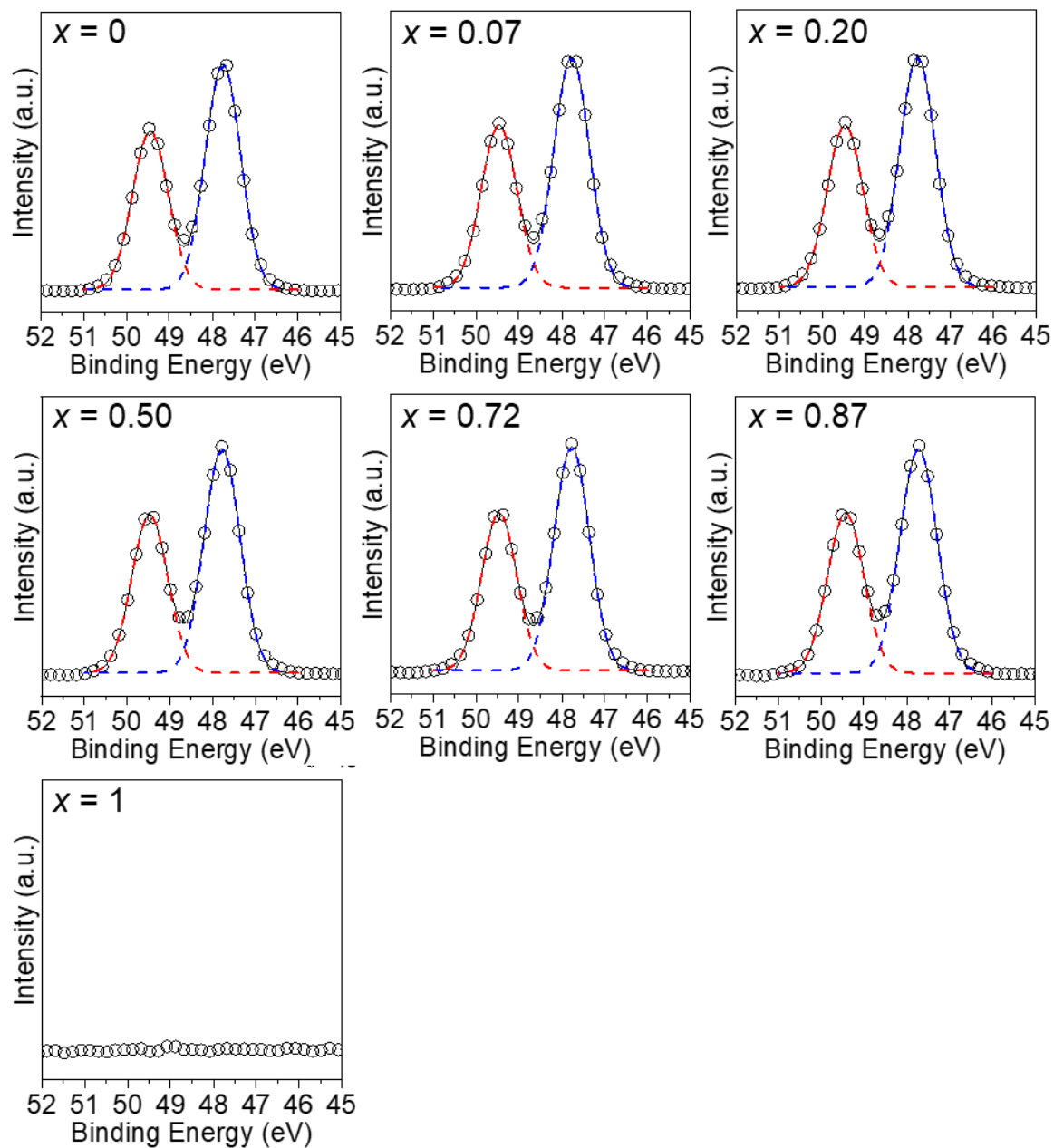


Figure S10. I 4d XPS spectra of  $\text{MAPb}(\text{I}_{1-x}\text{Br}_x)_3$  polycrystalline films ( $x = 0\text{--}1$ ).

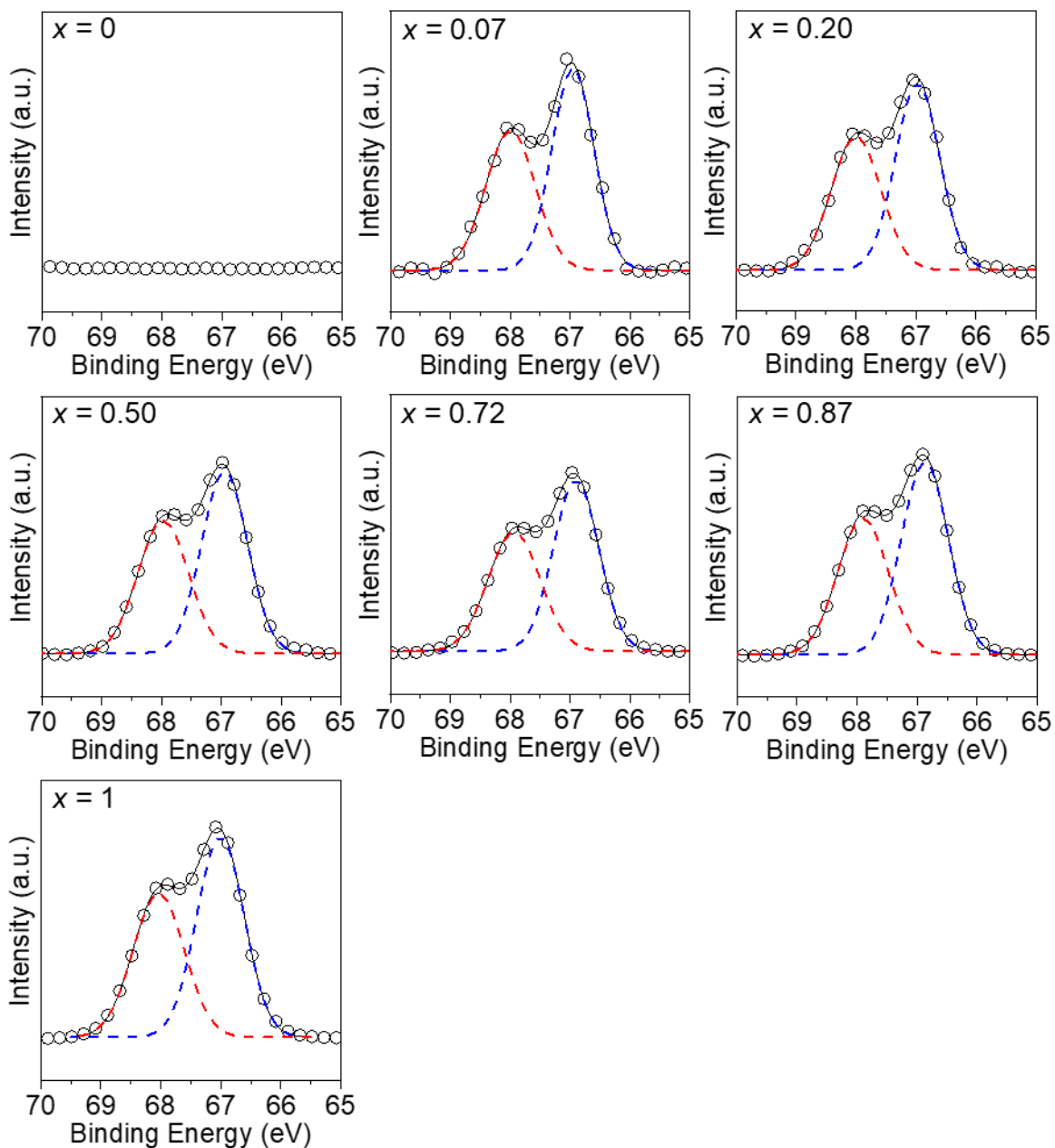


Figure S11. Br 3d XPS spectra of MAPb(I<sub>1-x</sub>Br<sub>x</sub>)<sub>3</sub> polycrystalline films ( $x = 0\text{--}1$ ).

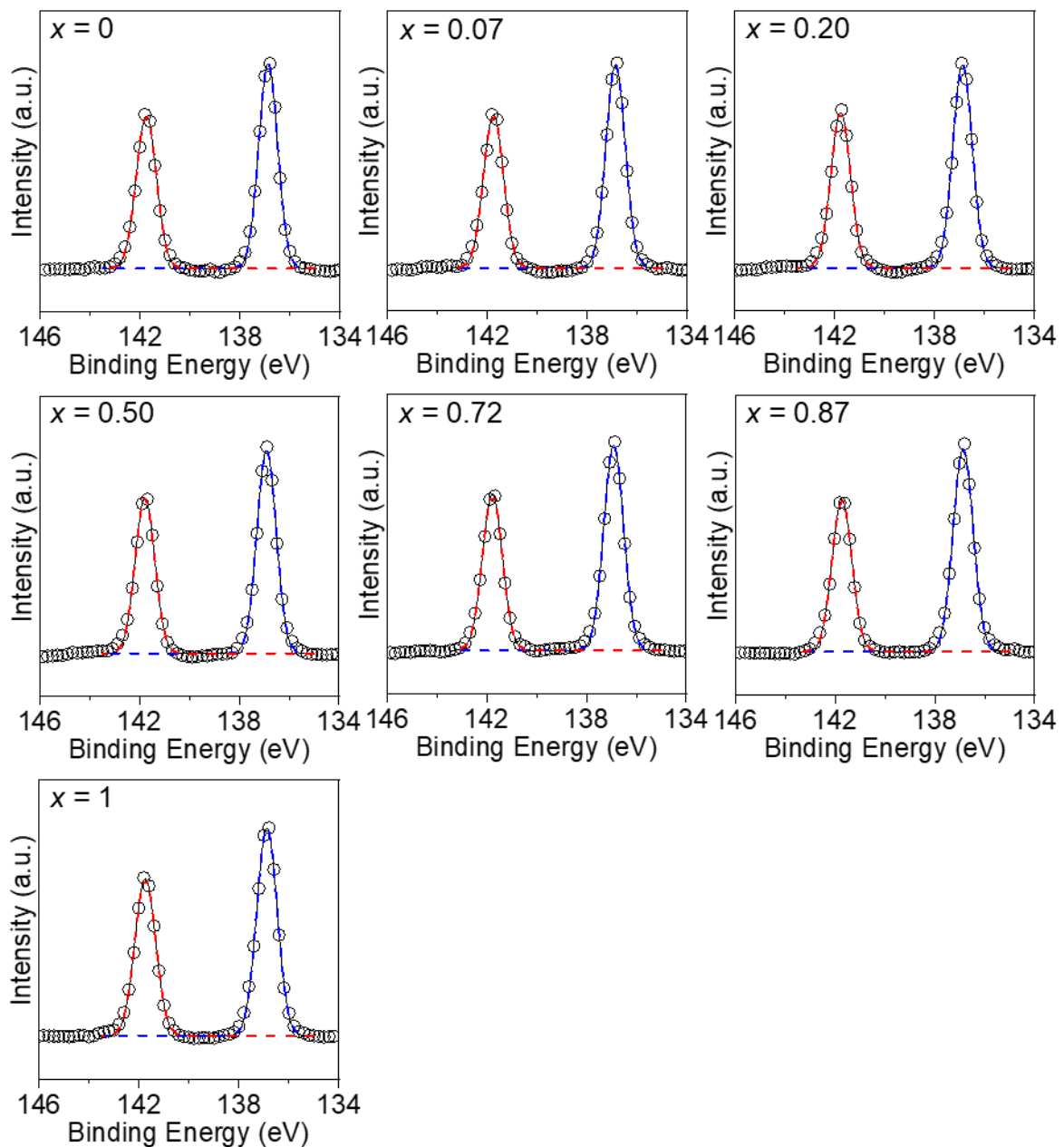


Figure S12. Pb 4f XPS spectra of  $\text{MAPb}(\text{I}_{1-x}\text{Br}_x)_3$  polycrystalline films ( $x = 0\text{--}1$ ).

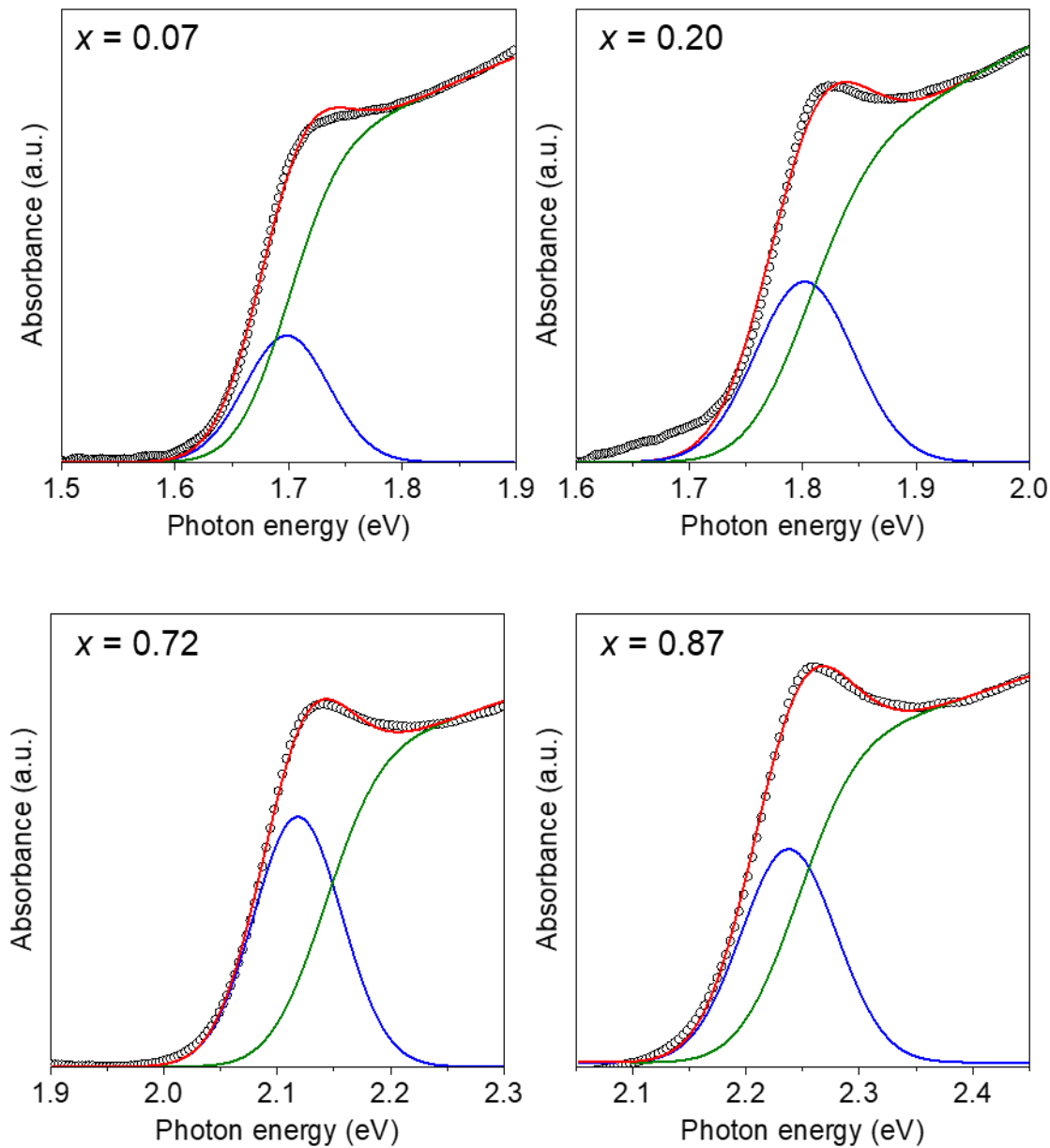


Figure S13. Absorption spectra of MAPb(I<sub>1-x</sub>Br<sub>x</sub>)<sub>3</sub> polycrystalline films ( $x = 0\text{--}1$ , determined from lattice parameters); experimental data measured at room temperature (296 K) ( $\circ$ ), total absorption (red solid line), absorption originating from exciton (blue solid line) and continuum contribution (green solid line).

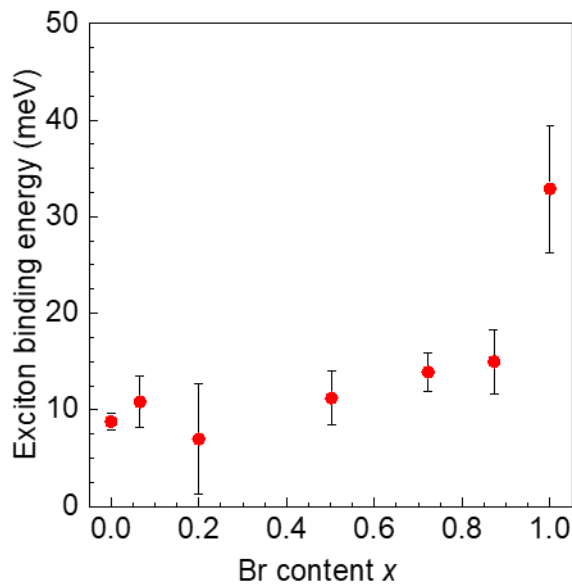


Figure S14. Exciton binding energies of  $\text{MAPb}(\text{I}_{1-x}\text{Br}_x)_3$  determined using absorption spectra of polycrystalline films ( $x = 0\text{--}1$ ) measured at room temperature (296 K).

## Reference

- 1 Noh, J. H.; Im, S. H.; Heo, J. H.; Mandal, T. N.; Seok, S. I. Chemical management for colorful, efficient, and stable inorganic-organic hybrid nanostructured solar cells. *Nano Lett.* **2013**, *13*, 1764–1769.
- 2 Kulkarni, S. A.; Baikie, T.; Boix, P. P.; Yantara, N.; Mathews, N.; Mhaisalkar, S. Band-gap tuning of lead halide perovskites using a sequential deposition process. *J. Mater. Chem. A* **2014**, *2*, 9221–9225.
- 3 Sadhanala, A.; Deschler, F.; Thomas, T. H.; Dutton, S. E.; Goedel, F. C.; Hanusch, F. C.; Lai, M. L.; Steiner, U.; Bein, T.; Docampo, P.; Cahen, D.; Friend, R. H. Preparation of Single-Phase Films of  $\text{CH}_3\text{NH}_3\text{Pb}(\text{I}_{1-x}\text{Br}_x)_3$  with Sharp Optical Band Edges. *J. Phys. Chem. Lett.* **2014**, *5*, 2501–2505.
- 4 Fedeli, P.; Gazza, F.; Calestani, D.; Ferro, P.; Besagni, T.; Zappettini, A.; Calestani, G.; Marchi, E.; Ceroni, P.; Mosca, R. Influence of the Synthetic Procedures on the Structural and Optical Properties of Mixed-Halide (Br, I) Perovskite Films. *J. Phys. Chem. C* **2015**, *119*, 21304–21313.

- 5 Atourki, L.; Vega, E.; Marí, B.; Mollar, M.; Ahsaine, H. A.; Bouabid, K.; Ihlal, A. Role of the chemical substitution on the structural and luminescence properties of the mixed halide perovskite thin  $\text{MAPbI}_{3-x}\text{Br}_x$  ( $0 \leq x \leq 1$ ) films. *Appl. Surf. Sci.* **2016**, *371*, 112–117.
- 6 Misra, R. K.; Ciammaruchi, L.; Aharon, S.; Mogilyansky, D.; Etgar, L.; Visoly-Fisher, I.; Katz, E. A. Effect of Halide Composition on the Photochemical Stability of Perovskite Photovoltaic Materials. *ChemSusChem* **2016**, *9*, 2572–2577.
- 7 Wang, W.; Su, J.; Zhang, L.; Lei, Y.; Wang, D.; Lu, D.; Bai, Y. Growth of mixed-halide perovskite single crystals. *CrystEngComm* **2018**, *20*, 1635–1643.
- 8 Zhang, Y.; Liu, Y.; Li, Y.; Yang, Z.; Liu, S.; Perovskite  $\text{CH}_3\text{NH}_3\text{Pb}(\text{Br}_x\text{I}_{1-x})_3$  single crystals with controlled composition for fine-tuned bandgap towards optimized optoelectronic applications. *J. Mater. Chem. C* **2016**, *4*, 9172–9178.
- 9 Yang, B.; Ming, W.; Du, M.-H.; Keum, J. K.; Puretzky, A. A.; Rouleau, C. M.; Huang, J.; Geohegan, D. B.; Wang, X.; Xiao, K. Real-Time Observation of Order-Disorder Transformation of Organic Cations Induced Phase Transition and Anomalous Photoluminescence in Hybrid Perovskites. *Adv. Mater.* **2018**, *30*, 1705801.
- 10 López, C. A.; Martínez-Huerta, M. V.; Alvarez-Galván, M. C.; Kayser, P.; Gant, P.; Castellanos-Gómez, A.; Fernández-Díaz, M. T.; Fauth, F.; Alonso, J. A. Elucidating the Methylammonium (MA) Conformation in  $\text{MAPbBr}_3$  Perovskite with Application in Solar Cells. *Inorg. Chem.* **2017**, *56*, 14214–14219.
- 11 Dang, Y.; Zhou, Y.; Liu, X.; Ju, D.; Xia, S.; Xia, H.; Tao, X. Formation of Hybrid Perovskite Tin Iodide Single Crystals by Top-Seeded Solution Growth. *Angew. Chem. Int. Ed.* **2016**, *55*, 3447–3450.